HUBBLE SPACE TELESCOPE COMBINED STRONG AND WEAK LENSING ANALYSIS OF THE CLASH SAMPLE: MASS AND MAGNIFICATION MODELS AND SYSTEMATIC UNCERTAINTIES

Adi Zitrin[1,18], Agnese Fabris[2], Julian Merten[1,3], Peter Melchior[4], Massimo Meneghetti[3], Anton Koekemoer[5], Dan Coe[5], Matteo Maturi[2], Matthias Bartelmann[2], Marc Postman[5], Keiichi Umetsu[6], Gregor Seidel[7], Irene Sendra[8], Tom Broadhurst[8,9], Italo Balestra[10], Andrea Biviano[10], Claudio Grillo[11], Amata Mercurio[12], Mario Nonino[10], Piero Rosati[13], Larry Bradley[5], Mauricio Carrasco[2], Megan Donahue[14], Holland Ford[15], Brenda L. Frye[16], and John Moustakas[17]

[1] Cahill Center for Astronomy and Astrophysics, California Institute of Technology, MC 249-17, Pasadena, CA 91125, USA; adizitrin@gmail.com
[2] Institut für Theoretische Astrophysik, Universität Heidelberg, Zentrum für Astronomie, Philosophenweg 12, D-69120 Heidelberg, Germany
[3] Jet Propulsion Laboratory, California Institute of Technology, Pasadena, CA 91109, USA
[4] Center for Cosmology and Astro-Particle Physics and Department of Physics, The Ohio State University, Columbus, OH 43210, USA
[5] Space Telescope Science Institute, 3700 San Martin Drive, Baltimore, MD 21218, USA
[6] Institute of Astronomy and Astrophysics, Academia Sinica, P.O. Box 23-141, Taipei 10617, Taiwan
[7] Max-Planck-Institut für Astronomie, Königstuhl 17, D-69117 Heidelberg, Germany
[8] Department of Theoretical Physics, University of Basque Country UPV/EHU, E-48080 Bilbao, Spain
[9] IKERBASQUE, Basque Foundation for Science, E-48011 Bilbao, Spain
[10] INAF/Osservatorio Astronomico di Trieste, via G.B. Tiepolo 11, I-34143 Trieste, Italy
[11] Dark Cosmology Centre, Niels Bohr Institute, University of Copenhagen, Juliane Maries Vej 30, DK-2100 Copenhagen, Denmark
[12] INAF/Osservatorio Astronomico di Capodimonte, via Moiariello 16, I-80131 Napoli, Italy
[13] Department of Physics and Earth Science, University of Ferrara, Via G. Saragat, I-44122 Ferrara, Italy
[14] Department of Physics and Astronomy, Michigan State University, East Lansing, MI 48824, USA
[15] Department of Physics and Astronomy, Johns Hopkins University, Baltimore, MD 21218, USA
[16] Steward Observatory, Department of Astronomy, University of Arizona, 933 N. Cherry Avenue, Tucson, AZ 85721, USA
[17] Department of Physics and Astronomy, Siena College, 515 Loudon Road, Loudonville, NY 12211, USA

ABSTRACT

We present results from a comprehensive lensing analysis in *Hubble Space Telescope* (*HST*) data of the complete Cluster Lensing And Supernova survey with Hubble cluster sample. We identify previously undiscovered multiple images, allowing improved or first constraints on the cluster inner mass distributions and profiles. We combine these strong lensing constraints with weak lensing shape measurements within the *HST* field of view (FOV) to jointly constrain the mass distributions. The analysis is performed in two different common parameterizations (one adopts light-traces-mass for both galaxies and dark matter while the other adopts an analytical, elliptical Navarro–Frenk–White form for the dark matter) to provide a better assessment of the underlying systematics—which is most important for deep, cluster-lensing surveys, especially when studying magnified high-redshift objects. We find that the typical (median), relative systematic differences throughout the central FOV are ∼40% in the (dimensionless) mass density, κ, and ∼20% in the magnification, μ. We show maps of these differences for each cluster, as well as the mass distributions, critical curves, and two-dimensional (2D)-integrated mass profiles. For the Einstein radii ($z_s = 2$) we find that all typically agree within 10% between the two models, and Einstein masses agree, typically, within ∼15%. At larger radii, the total projected, 2D-integrated mass profiles of the two models, within $r \sim 2'$, differ by ∼30%. Stacking the surface-density profiles of the sample from the two methods together, we obtain an average slope of $d \log(\Sigma)/d \log(r) \sim -0.64 \pm 0.1$, in the radial range [5350] kpc. Last, we also characterize the behavior of the average magnification, surface density, and shear differences between the two models as a function of both the radius from the center and the best-fit values of these quantities. All mass models and magnification maps are made publicly available for the community.

Key words: galaxies: clusters: general – galaxies: high-redshift – gravitational lensing: strong – gravitational lensing: weak

Supporting material: extended figures, machine-readable table

1. INTRODUCTION

Lensing by galaxy clusters has become of great interest, due to the inherent ability to constrain the underlying matter distribution of the lens, dominated by an *unseen* dark matter (DM) component, and thanks to the magnification effect that distorts and enhances faint background objects to be detected through such cosmic lenses (e.g., Bartelmann 2010; Kneib & Natarajan 2011, for recent reviews).

Background galaxies lensed by galaxy clusters are magnified in size and flux and get distorted and sheared as a consequence of the cluster's gravitational potential. In recent years, the inner parts of galaxy clusters have been mapped with increasing precision, particularly through the strong lensing (SL) phenomenon in which background galaxies are also multiply imaged, allowing for high-resolution constraints to be placed on the mass distribution and profile (Kneib et al. 2004; Broadhurst et al. 2005; Smith et al. 2005; Limousin et al. 2008; Newman et al. 2009; Richard et al. 2010, 2014; Bradač et al. 2008; Liesenborgs et al. 2008; Diego et al. 2005, 2015b, 2015a; Coe et al. 2010; Oguri et al. 2013; Sereno et al. 2013; Zitrin et al. 2009b,

---

2011a, 2013a; Jauzac et al. 2014; Grillo et al. 2014, as some examples). In particular, this improvement is attributed to the remarkable spatial resolution and image quality of the *Hubble Space Telescope* (*HST*), which has allowed the detection of many multiple-image constraints in clusters, as reflected in the works mentioned above. This has become well-acknowledged, motivating substantial cluster-lensing surveys, such as the Cluster Lensing and Supernova survey with Hubble (CLASH; Postman et al. 2012), in which 25 clusters were observed in 16 filters, so that many multiple images could be found and their redshifts well-determined, allowing mapping of the cluster mass distributions with great precision; or the Hubble Frontier Fields program (HFF),[19] set to observe four to six massive clusters to an unprecedented depth, to exploit their magnification power (and our ability to map it through lensing) and study very high-z galaxies (Atek et al. 2014a, 2014b; Coe et al. 2014; Ishigaki et al. 2015; Laporte et al. 2014; Zheng et al. 2014; Zitrin et al. 2014; see also Lotz et al. 2014).

Further outward from the cluster core, where the density is typically lower than the critical density for SL (see Narayan & Bartelmann 1996), background objects observed through the lensing cluster will be (only) slightly sheared and magnified, an effect that could be detected, in principle, only on a statistical basis due to the intrinsic scatter in their source ellipticities (Kaiser et al. 1995; Bartelmann & Schneider 2001; Hoekstra & Jain 2008). This weak lensing (WL) effect is thus used to map the mass distribution (or profile) out to the virial radius and beyond, allowing a large-scale view of the cluster and surrounding structures (e.g., Merten et al. 2009; Umetsu et al. 2009, 2010, 2012; Okabe et al. 2010; Jauzac et al. 2012; Medezinski et al. 2013).

Among the main goals of the CLASH program is addressing some standing questions related to structure formation in the context of the standard ΛCDM paradigm. Accurate mass maps for the clusters can be exploited for characterizing with unprecedented precision the observational concentration–mass relation and Einstein radius distribution, for example, both of which have been previously claimed to be in some tension with predictions from semianalytic calculations or simulations based on ΛCDM (e.g., Broadhurst & Barkana 2008; Broadhurst et al. 2008; Zitrin et al. 2010, 2011a; Meneghetti et al. 2011).

Various studies have previously combined SL+WL (e.g., Bradač et al. 2006; Limousin et al. 2007; Merten et al. 2009, 2011; Umetsu et al. 2011a, 2011b, 2012; Oguri et al. 2012; Newman et al. 2013a, 2013b). These, however, are often made either (1) independently (i.e., after the fact, so that each regime is first used to construct a mass model, regardless of the other regime's constraints); (2) nonparametrically, meaning without any assumptions on the mass distribution or use of a parameterized model, but using a (usually lower-resolution) free-form grid instead; or (3) using wide-field ground-based imaging for the WL regime. Here, we aim to combine the two effects for a simultaneous fit in the *HST* data alone (e.g., Kneib et al. 1996; Smith et al. 2005; Richard et al. 2014), through a joint minimization of a high-resolution parametric model. Although the *HST* field of view (FOV) is smaller than typical wide-field imaging, its remarkable resolution allows for shape measurements of a higher number density of background galaxies (e.g., Kneib et al. 1996; Merten et al. 2014). Moreover, we perform the fit with two distinct parameterizations and so

quantify and characterize the underlying systematic differences between them.[20] This quantification, especially on a substantial sample, is a great leap forward in estimating the true errors on lens modeling and is most important in the era of precision cosmology and designated deep cluster surveys aiming to study the magnified high-z Universe through cluster lenses, such as the HFF.

We jointly analyze the SL and WL signals in the central *HST* FOV of the complete sample of 25 galaxy clusters observed recently in the CLASH program. All mass models presented in this work are being made publicly available to the astronomical community through the Mikulski Archive for Space Telescopes (MAST) as a CLASH high-end science product[21]. The models we release include *.*fits* file scalable maps of the deflection fields, projected mass density, magnification, and shear components, as well as their error maps. In addition, the multiple-image identification or catalogs we list here (Table 2) can be used for future independent modeling in other techniques to compare to our current findings. In subsequent works (K. Umetsu et al., in preparation; M. Meneghetti et al., in preparation), we aim to use the models presented here to compare the overall statistical properties of the sample (such as the concentration–mass relation, or the Einstein radius distribution), with predictions by ΛCDM. In fact, as part of our broad effort to characterize structure formation, CLASH has recently published the most up-to-date concentration–mass relation from wide-field SL+WL nonparametric joint analysis, while comparing it to numerical simulations (Merten et al. 2014; Meneghetti et al. 2014), and published independent WL (Umetsu et al. 2014) and X-ray (Donahue et al. 2014) analyses for the majority of the sample. Our following analysis concentrates on high-resolution mass and magnification mapping of the cluster cores for the full CLASH sample.

The paper is organized as follows: In Section 2 we summarize the observations and data reduction, including shape measurements. In Section 3 we outline the lens modeling techniques we use here and their application to the CLASH clusters. In Section 4 we briefly summarize the analysis per cluster, where the full sample modeling results are presented and discussed in Section 5 along with the revealed systematic uncertainties or differences between the two modeling methods. The work is summarized and concluded in Section 6. Throughout the work we use standard ΛCDM cosmology with ($\Omega_{m0} = 0.3$, $\Omega_{\Lambda0} = 0.7$, $H_0 = 100\ h\,\mathrm{km\,s^{-1}\,Mpc^{-1}}$, with $h = 0.7$). We often also abbreviate *Abell* clusters (e.g., Abell et al. 1989) with "A," and MACS clusters (MAssive Cluster Survey; e.g., Ebeling et al. 2001, 2010) with "M," etc.

2. DATA AND OBSERVATIONS

Each of the 25 CLASH clusters was observed with *HST*, generally in 16 filters ranging from the UVIS, through the optical into the near-IR, using the Wide Field Camera 3 and Advanced Camera for Surveys (ACS) cameras. Each cluster was observed to a depth of ∼15–20 orbits during *HST*'s cycles 18, 19, or 20, often supplementing some existing observations. For full details, we refer the reader to Postman et al. (2012). Cluster redshifts are mainly taken from Postman et al. (2012), and references therein, although slight (and negligible for our purposes) discrepancies

---

[19] http://www.stsci.edu/hst/campaigns/frontier-fields/

[20] Note that throughout we may refer to these differences simply as "systematics" or "systematic uncertainties," where the meaning remains the systematic differences between these two specific methods (but can be regarded more generally as a case study of systematic uncertainties in lens modeling).

[21] http://archive.stsci.edu/prepds/clash/

may apply, e.g., due to different round-ups, revision with new spectroscopic data, or later literature.

The SL constraints, namely, the positions of multiple images and their redshift information, were adopted from previous works where available and are often complemented here with newly uncovered sets. New multiple images were generally uncovered here with the aid of a preliminary model constructed for each cluster using the Zitrin et al. (2009b) method, with the assumption that light-traces-mass (LTM hereafter; see Section 3.1), so that these multiple images are not simply chosen by eye but are also predicted physically by a preliminary light-tracing model. For some of these we present first spectroscopic measurements taken by the CLASH-VLT campaign (PI: Rosati). For the multiple images that lack spectroscopic data to date, we typically adopt the multiband photometric redshift from the CLASH pipeline that incorporates the Bayesian photometric redshift (BPZ) software (Benítez 2000; Coe et al. 2006; see also Jouvel et al. 2014 for CLASH photo-z accuracy), although often some of these redshifts we leave as free parameters to be optimized in the minimization procedure, as we shall specify for each cluster separately (e.g., Tables 1 and 2). In Section 4 we also include additional brief background, such as previous analyses, multiple images, the ellipticity catalog, or other notable features stemming from our current analysis, upon relevancy.

For the *HST* WL shape measurements, we produced images with $0\rlap{.}''03$ pixel^{-1} by drizzling each visit in the unrotated frame of the ACS detector, using a modified version of the "Mosaicdrizzle" pipeline (described more fully in Koekemoer et al. 2011). This allows accurate point-spread function (PSF) treatment that does not compromise the intrinsic shape measurements required by WL pipelines. The RRG (Rhodes et al. 2000) WL shape measurement package was then used to measure shapes in each of six ACS bands (F435W, F475W, F625W, F775W, F814W, and F850LP). The RRG pipeline corrects for the Hubble PSF by determining the telescope's focus offset from the nominal value. The focus offset is determined by the inspection of stellar ellipticities in the full field and by cross-checking with the STScI focus tool[22] for each visit's image. From the focus offset, a PSF model is created based on Rhodes et al. (2007), and shape measurements are corrected accordingly (see Rhodes et al. 2000, 2007; Merten et al. 2014, for more details).

We exclude objects with signal-to-noise ratio (S/N) < 10 and size $<0\rlap{.}''1$ because faint or poorly resolved galaxies are known to yield very inaccurate shape measurements. All the shape catalogs were then matched to the deep multiband photometric catalog, and for objects that were successfully measured in more than a single filter, the ellipticities were combined by an S/N-weighted average to reduce the measurement noise. A selection for lensed background galaxies is achieved by choosing galaxies with a minimum photometric redshift estimate $\min(z_b) = z_c + 0.2$, such that the cluster redshift z_c is well below the 95% confidence region of the BPZ redshift distribution. Due to the faintness of the objects, no BPZ quality cuts were applied.

In Section 3 we now describe the lens-modeling pipeline.

3. LENS MODELING

For the combined SL+WL analysis we use a revised version of the Zitrin et al. (2009b, 2013a, 2013b) SL modeling technique, extended here to also include WL shape measurements for joint minimization throughout the *HST*/ACS frame. The lens-modeling code includes two different parameterizations, which

we use here to examine the credibility of the resulting mass and magnification models and to assess the underlying systematic uncertainties or differences between them. We give here a brief review of these techniques, including the extension to the WL regime, but refer the reader to the above works for further details were these required.

3.1. Light-traces-mass

The first method we use here adopts the assumption that the mass distribution of both the galaxies *and* DM is reasonably traced by the cluster's light distribution (Broadhurst et al. 2005). The first component of the mass model is the superposition of all cluster galaxies, each modeled by a power-law surface mass–density profile, scaled by its luminosity. The exponent of this power law, q, is the same for all galaxies, yet is a free parameter in the minimization and thus is iterated for in each cluster. The resulting galaxies' mass map is then smoothed, using a two-dimensional (2D) Gaussian, to represent the smoother, DM component (there is an option to use a 2D Spline interpolation smoothing instead). The Gaussian width (or polynomial degree), S, is the second free parameter of the model. The two components are then simply added with a relative weight, $k_{\rm gal}$, which is also left free to be optimized by the minimization procedure. To allow for further flexibility, a two-component external shear is then added. The amplitude and direction of the external shear are two additional free parameters. The overall normalization of the model, $K_{\rm norm}$, is the final, free fundamental parameter. The modeling thus includes only six free fundamental parameters. The minimal number of parameters, but more so, the reasonable assumption that LTM, *readily* allows for the detection of multiple-image sets (Broadhurst et al. 2005; Zitrin et al. 2009a, 2009b, 2013a, 2013b, as a few examples,).

In addition, to allow for further flexibility and because not all galaxies are expected to have the exact same mass-to-light ratio, one can allow the weight of chosen galaxies to be optimized in the minimization. Additionally, ellipticity and, independently, a core, can be added to specified galaxies. In fact, as a rule of thumb, we generally make use here of this feature and assign to the BCG its measured ellipticity value from SExtractor.

The best-fit model, parameter values, and errors are obtained by a dozen to several dozen thousand Monte Carlo Markov Chain (MCMC) steps. The goodness-of-fit criteria for the SL regime is embedded in the form of a χ^2 of the position of multiple images:

$$\chi^2_{SL} = \sum_i \frac{(x'_i - x_i)^2 + (y'_i - y_i)^2}{\sigma^2_{\rm pos}}, \qquad (1)$$

where $[x_i, y_i]$ is the position of the ith multiple image; $[x'_i, y'_i]$ is the position of the ith multiple image predicted by the model; and we take throughout a positional uncertainty of $\sigma_{\rm pos} = 0\rlap{.}''5$ (see, e.g., Newman et al. 2013b).

3.2. PIEMD + eNFW

The second method we use here adopts the LTM assumption only for the galaxy component, whereas the DM component is obtained by adopting a symmetric, analytic form. Here, cluster galaxies are each modeled as a Pseudo-Isothermal Elliptical Mass Distribution (PIEMD) scaled by its luminosity (although note that as for the LTM model, typically we do not incorporate ellipticities for the cluster galaxies aside for the BCGs).

Table 1
Summary of Analysis Results

Cluster$_{model}$	Free Gals	Free Reds	χ^2_{SL}	χ^2_{WL}	χ^2/DOF	N_p	N^c_{SL}	N^c_{WL}	z_{WL}	rms	ln(ev)	θ_e	M_e	M_{2D} ($< \theta \simeq 2\rlap{.}'3$)
A209$_{LTM}$	1	2	117.2	1268.1	1385.3/1609 = 0.86	11	8	1612	0.95	2.05	−694.6	9.0	0.82	1.97
A209$_{NFW}$	1	2	43.4	1262.9	1306.4/1611 = 0.81	9	8	1612	0.95	1.25	−648.8	8.9	0.75	2.19
A383$_{LTM}$	2	0	152.8	1333.7	1486.5/1602 = 0.93	10	22	1590	1.14	1.50	−705.0	15.2	2.13	2.39
A383$_{NFW}$	2	0	93.7	1330.0	1423.6/1600 = 0.89	12	22	1590	1.14	1.17	−679.3	15.0	2.08	1.60
A611$_{LTM}$	1	1	88.8	836.0	924.8/1111 = 0.83	9	26	1094	0.86	1.14	−460.4	18.9	4.70	5.67
A611$_{NFW}$	1	1	58.3	836.9	895.2/1112 = 0.81	8	26	1094	0.86	0.93	−445.4	17.2	4.08	3.45
A1423$_{LTM}$	1	0	1.6	1286.2	1287.8/1603 = 0.80	7	2	1608	0.92	0.45	−690.4	19.6	3.85	3.00
A1423$_{NFW}$	0	0	3.4	1284.0	1287.4/1604 = 0.80	6	2	1608	0.92	0.65	−660.9	17.6	3.24	1.78
A2261$_{LTM}$	1	6	76.7	1119.9	1196.6/1440 = 0.83	16	20	1436	0.79	1.06	−596.9	22.9	5.65	4.05
A2261$_{NFW}$	1	6	50.6	1121.8	1172.4/1441 = 0.81	15	20	1436	0.79	0.86	−573.1	23.4	6.04	3.43
CL1226$_{LTM}$	2	1	131.4	2398.7	2530.1/1686 = 1.50	10	20	1676	0.99	1.53	−1131.5	14.5	8.09	8.14
CL1226$_{NFW}$	2	2	40.1	2400.5	2440.6/1680 = 1.45	14	18	1676	0.99	0.88	−1071.6	14.1	8.73	9.77
M0329$_{LTM}$	2	1	69.9	861.4	931.3/987 = 0.94	9	16	980	1.18	1.26	−436.9	22.8	10.32	7.73
M0329$_{NFW}$	3	1	91.6	862.0	953.6/982 = 0.97	14	16	980	1.18	1.44	−449.0	25.4	13.37	7.09
M0416$_{LTM}$	7	11	425.3	955.0	1380.3/1122 = 1.23	24	44	1102	1.16	1.72	−962.3	25.0	10.35	10.52
M0416$_{NFW}$	7	11	348.9	961.1	1310.0/1117 = 1.17	29	44	1102	1.16	1.56	−678.1	26.7	12.42	8.50
M0429$_{LTM}$	1	0	35.2	1069.7	1104.9/1304 = 0.85	8	10	1302	1.08	1.12	−559.4	15.1	4.15	7.66
M0429$_{NFW}$	1	0	5.4	1064.8	1070.2/1305 = 0.82	7	10	1302	1.08	0.44	−516.4	16.2	4.97	3.78
M0647$_{LTM}$	2	4	133.5	1336.8	1470.2/1537 = 0.96	13	22	1528	1.14	1.40	−755.2	26.3	17.24	11.21
M0647$_{NFW}$	2	4	448.4	1337.1	1785.4/1538 = 1.16	12	22	1528	1.14	2.57	−891.0	26.4	19.18	10.36
M0717$_{LTM}$	10	9	1858.7	962.0	2820.7/1045 = 2.70	25	62	1008	1.04	3.18	−1390.0	$\simeq$55	233.85	20.31
M0744$_{LTM}$	2	3	56.1	1359.7	1415.8/1488 = 0.95	12	16	1484	1.32	1.00	−717.7	25.3	20.70	14.15
M0744$_{NFW}$	1	3	164.8	1360.9	1525.7/1486 = 1.03	14	16	1484	1.32	1.72	−740.6	23.3	19.26	8.15
M1115$_{LTM}$	1	1	48.8	873.6	922.5/975 = 0.95	9	12	972	1.03	1.16	−456.5	17.8	4.99	7.62
M1115$_{NFW}$	1	1	50.4	866.5	916.9/976 = 0.94	8	12	972	1.03	1.18	−451.4	18.5	5.69	5.26
M1149$_{LTM}$	7	9	820.2	1458.7	2278.9/1706 = 1.34	22	68	1660	0.99	2.01	−1072.5	20.4	9.83	14.36
M1206$_{LTM}$	5	5	335.5	989.4	1324.9/1203 = 1.10	17	58	1162	1.13	1.45	−675.7	26.3	13.24	9.30
M1206$_{NFW}$	2	5	483.8	986.0	1469.8/1207 = 1.22	13	58	1162	1.13	1.74	−695.4	27.3	15.31	9.26
M1311$_{LTM}$	1	0	9.6	758.6	768.2/892 = 0.86	8	6	894	1.03	0.69	−369.7	13.5	4.24	8.96
M1311$_{NFW}$	1	1	2.8	760.3	763.1/892 = 0.86	8	6	894	1.03	0.37	−361.6	14.8	5.09	5.66
M1423$_{LTM}$	1	1	111.4	1684.3	1795.7/1803 = 1.00	9	28	1784	1.04	1.21	−824.1	17.6	7.55	10.93
M1423$_{NFW}$	1	1	164.8	1693.2	1858.0/1804 = 1.03	8	28	1784	1.04	1.47	−853.6	17.8	8.20	6.13
RXJ1532$_{LTM}$	1	0	12.0	852.3	864.3/1004 = 0.86	8	2	1010	1.07	1.22	−417.5	9.0	1.38	5.35
RXJ1532$_{NFW}$	1	0	1.4	850.7	852.1/1004 = 0.85	8	2	1010	1.07	0.41	−411.5	10.5	1.85	3.09
M1720$_{LTM}$	1	4	83.9	1112.4	1196.3/1272 = 0.94	12	20	1264	1.11	1.15	−642.4	20.4	7.22	7.15
M1720$_{NFW}$	1	4	253.9	1120.3	1374.2/1273 = 1.08	11	20	1264	1.11	1.99	−643.6	19.8	7.36	3.35
M1931$_{LTM}$	1	2	249.2	797.2	1046.4/1422 = 0.74	10	16	1416	0.82	2.28	−538.2	22.7	8.32	6.07
M1931$_{NFW}$	1	2	28.5	791.2	819.6/1423 = 0.58	9	16	1416	0.82	0.77	−461.0	21.8	7.82	4.57
M2129$_{LTM}$	1	6	560.0	1590.6	2150.7/1718 = 1.25	16	32	1702	1.23	2.42	−950.4	19.2	9.23	11.85
M2129$_{NFW}$	1	6	333.1	1597.3	1930.4/1721 = 1.12	13	32	1702	1.23	1.86	−846.7	21.8	12.99	8.59
MS2137$_{LTM}$	1	0	51.4	1619.6	1671.0/1572 = 1.06	8	10	1570	1.12	1.27	−790.7	17.2	4.45	3.32
MS2137$_{NFW}$	1	0	19.1	1622.3	1641.3/1573 = 1.04	7	10	1570	1.12	0.77	−779.3	17.0	4.42	2.69
RXJ1347$_{LTM}$	2	4	490.2	1246.3	1736.6/1276 = 1.36	14	24	1266	1.13	2.61	−738.1	33.3	22.65	18.04
RXJ1347$_{NFW}$	2	4	276.5	1251.3	1527.8/1274 = 1.20	16	24	1266	1.13	1.96	−687.9	32.7	22.11	14.99
RXJ2129$_{LTM}$	1	4	88.5	1034.7	1123.1/1198 = 0.94	12	18	1192	0.82	1.26	−522.8	13.3	1.85	3.39
RXJ2129$_{NFW}$	1	4	17.9	1036.4	1054.3/1199 = 0.88	11	18	1192	0.82	0.57	−491.7	12.6	1.63	2.01
RXJ2248$_{LTM}$	1	14	318.8	923.2	1242.0/1216 = 1.02	22	58	1180	1.12	1.35	−662.3	31.1	13.52	10.33
RXJ2248$_{NFW}$	1	14	547.0	942.7	1489.7/1217 = 1.22	21	58	1180	1.12	1.76	−732.2	31.1	15.74	8.35

Notes. *Column 1:* abbreviated cluster name (see Section 4 and Postman et al. 2012 for more cluster details), including each method used for the analysis (LTM or PIEMDeNFW, the latter being abbreviated here as "NFW"; see Section 3 for details). *Column 2:* number of galaxies whose relative contribution to the deflection map (i.e., its mass-to-light ratio) is left to be optimized by the minimization procedure. *Column 3:* number of background sources whose redshift was left to be optimized by the minimization procedure. *Column 4:* χ^2 of the SL regime. *Column 5:* χ^2 of the WL regime. *Column 6:* reduced χ^2, χ^2/DOF. *Column 7:* total number of free parameters in our models. *Column 8:* number of effective SL constraints. *Column 9:* number of effective WL constraints. *Column 10:* mean effective redshift of the weakly lensed galaxies corresponding to the mean lensing depth $\langle\beta\rangle = \langle D_{ls}/D_s\rangle$ of the sample, defined as $\beta(\bar{z}_{eff}) = \langle\beta\rangle$. *Column 11:* image-plane reproduction rms in arcseconds. *Column 12:* natural logarithm of the Bayesian evidence, calculated following the approximation given in Marshall et al. (2006). *Column 13:* effective Einstein radius for $z_s = 2$ in arcseconds ($\sqrt{A/\pi}$, where A is the area enclosed within the critical curves). *Column 14:* mass enclosed within the critical curves for $z_s = 2$, in [$10^{13}\,M_\odot$]. *Column 15:* 2D radially integrated mass within our analysis FOV, $\theta \simeq 136''$, in [$10^{14}\,M_\odot$] (see Figure 2).

Table 2
Multiple Images and Candidates

Arc ID	α (deg)	δ (deg)	Photo-z [95% C.I.]	Input z	z_{LTM} [95% C.I.]	z_{NFW} [95% C.I.]	Comments
				A209			
1.1	22.966446	−13.611836	1.13 [1.08, 1.23]	2.63	⋯	⋯	
1.2	22.967486	−13.610139	⋯	⋯	⋯	⋯	
1.3	22.970421	−13.608081	2.63 [2.49, 2.73]	⋯	⋯	⋯	
2.1	22.968694	−13.615574	0.64 [0.55, 0.69]	⋯	3.47 [2.97, 5.83]	0.77 [0.67, 0.85]	
2.2	22.967876	−13.616512	⋯	⋯	⋯	⋯	
3.1	22.967951	−13.615285	⋯	⋯	1.74 [1.74, 4.90]	4.78 [2.14, 6.21]	
3.2	22.968025	−13.616946	⋯	⋯	⋯	⋯	

Notes. *Column 1:* cluster-abbreviated name followed by its arcs' ID. "c" stands for candidate (for *candidates* the photo-z distribution or identification was ambiguous), and "p" stands for predicted location for notably missing counterimages (so that the absence of "p" does not necessarily mean that no other images are predicted), whereas an additional "?" sign indicates that various candidates are seen nearby and the detection is thus even more ambiguous, or that a candidate counterimage is seen but not necessarily predicted by the model. *Columns 2 & 3:* R.A. and decl. in J2000.0. *Column 4:* photometric redshift and 95% C.L. from the automated CLASH catalogs (best option among the IR and optical+IR catalogs automatically generated by CLASH). *Column 5:* input redshift adopted for each system. If a spectroscopic redshift is available we list it with a minus sign, along with its references in the *comments* column. Also, note that there may be some discrepancy between the best adopted redshift per system (which was more carefully chosen) and the mean photometric redshift from its multiple images given in the automated CLASH catalog. *Column 6:* predicted and 95% C.L. redshift by the LTM model. *Column 7:* predicted and 95% C.L. redshift by the PIEMDeNFW model. *Column 8:* comments/references.

(This table is available in its entirety in machine-readable form.)

The PIEMD prescription adopted follows Jullo et al. (2007; see also Zitrin et al. 2013a, 2013b). The DM component is modeled as an elliptical Navarro–Frenk–White (NFW; Navarro et al. 1996) mass–density distribution (eNFW hereafter). The velocity dispersion, σ_*, and the cut-off radius, $r_{\mathrm{cut},*}$, of a reference galaxy M_*, are the two free parameters of the galaxies' component. The DM component comprises four more fundamental free parameters: the mass and concentration, M_{200} and C_{200}, and the ellipticity and position angle, e and PA, where two additional parameters, namely, the 2D shift of the DM halo center from the BCG, can be added—although we usually do not make use of this feature and force the DM center to coincide with that of the BCG. Additionally, in complex, or merging, clusters, it is often required to add additional DM (i.e., eNFW here) halos to well reproduce the mass distribution (e.g., Smith et al. 2009; Limousin et al. 2012; Zitrin et al. 2013a, 2013b), where in our work here we limit the number of DM halos to two. For each cluster we specify in Section 4 additional details relevant for its specific analysis.

As above (Section 3.1), galaxies can be left freely weighted to be optimized by the model, and the minimization is similarly performed via a long MCMC with the same χ^2 definition (Equation (1)).

3.3. Weak Lensing Regime

To simultaneously fit for the SL and WL regimes, we add a term for the total χ^2 accounting also for the WL data, so that the total χ^2 is given by

$$\chi_{\mathrm{tot}}^2 = \chi_{\mathrm{SL}}^2 + \chi_{\mathrm{WL}}^2 \qquad (2)$$

with

$$\chi_{\mathrm{WL}}^2 = \sum_i \frac{(g'_{1,i} - g_{1,i})^2 + (g'_{2,i} - g_{2,i})^2}{\sigma_{\mathrm{ell}}^2}, \qquad (3)$$

where $g_{1,i}$ and $g_{2,i}$ are the two components of the measured, complex reduced shear of the ith galaxy; $g'_{1,i}$ and $g'_{2,i}$ are the

same two components as predicted by the model at each galaxy location; and σ_{ell} is the width of the distribution of measured ellipticities (which governs the error in reduced shear), typically ∼0.3, which we adopt here as our nominal value following measurements of the standard deviation of a few input, shape measurement catalogs (see also Chang et al. 2013; Newman et al. 2013b). While it is sometimes accustomed to use each background galaxy in the WL catalog individually, by using specifically the signal-to-noise ratio and photo-z of each galaxy, our tests while constructing the lens-modeling pipeline indicated that this has a negligible effect on the results, compared with using the fixed intrinsic ellipticity scatter we measured from our catalogs, or adopting the mean lensing depth, as we do here (see also Newman et al. 2013b for a similar conclusion).

We disregard, i.e., we do not take into account in the χ^2, galaxies for which the sign of the magnification by the lens model is negative, meaning that they lay inside the critical curves for the mean effective redshift of the WL sample. One also has to bear in mind that for background galaxies close to the cluster center, shape measurements may be affected by higher-order terms such as flexion. It is currently uncertain by how much flexion may actually affect one's shape measurements, a subject worthy of proper investigation in future studies. We note, however, that in Merten et al. (2014) the effect of flexion on shape measurements in our *HST* WL catalogs was found to be negligible—by comparing mass profiles constructed with and without the inclusion of background galaxies close to the cluster center, finding these are in excellent agreement. In addition, the RRG pipeline used here for shape measurements was found to correctly measure the reduced shear to within 1%, well into the SL regime (Massey & Goldberg 2008).

For completeness, we will also use throughout the *reduced* χ^2 and note that the overall number of degrees-of-freedom (DOF) in the lensing model is

$$\mathrm{DOF} = N_{\mathrm{SL,c}} + N_{\mathrm{WL,c}} - N_p, \qquad (4)$$

where N_p is the number of free parameters in the modeling, $N_{SL,c}$ is the number of SL constraints, and $N_{WL,c}$ is the number of WL constraints. $N_{SL,c}$ is given by

$$N_{SL,c} = \nu(N_{im} - N_s), \qquad (5)$$

where the number of dimensions is $\nu = 2$ because each image (and source) is characterized by two measures (e.g., x and y), N_{im} is the total number of images used for the fit, and N_s the number of systems (or sources; see also Kneib et al. 1993 for an equivalent formalism, or for an extension of the above to cases in which redshifts of background objects are also left to be freely optimized). From similar considerations, $N_{WL,c}$ is simply twice the number of galaxies used as constraints from our shape catalogs.

4. INDIVIDUAL CLUSTER ANALYSIS

In this section we briefly introduce each cluster in our sample, its lensing analysis, and notable results. Other technical or fitting results are summarized in Table 1, and the resulting maps are explicitly shown in the figures throughout this work.

4.1. A209

The galaxy cluster A209 ($z = 0.21$) is part of the main, relaxed cluster sample of the CLASH program. We found no record of a previous SL analysis of this cluster, nor any identification of multiple images outside the CLASH framework. A209 has been, however, the subject of various WL studies (Dahle et al. 2002; Smith et al. 2005; Paulin-Henriksson et al. 2007; Okabe et al. 2010; see also Merten et al. 2014; Umetsu et al. 2014 for the analysis of most of the CLASH sample).

Here, we find the first seven multiple images in this cluster, corresponding to three systems, which we consider as a secure set of constraints for the modeling. Our analysis therefore puts first constraints on the inner mass distribution of this cluster. We find a rather small lens, with an effective Einstein radius of $\sim 9''$ for $z_s = 2$, accounting for the small number of multiple images seen (also, two of the three systems found are locally lensed by a bright cluster member close—$\simeq 18''$—to the BCG). In our modeling we use the photometric redshift of system 1 as fixed and leave the redshifts of systems 2 and 3, as well as the relative weight of the BCG, to be optimized by the MCMC. In the LTM case we also left the PA of the BCG and its core radius to be freely weighted. Our WL shape measurements include 806 galaxies that lay outside the critical curves and are used for the WL constraints. The results are summarized in Table 1 and seen in the figures throughout.

4.2. A383

A383 ($z = 0.189$) was the first cluster we analyzed in the CLASH framework (Zitrin et al. 2011b). SL features used here were known from previous works, spanning the redshift range $z = [1, 6]$ (e.g., Smith et al. 2001; Sand et al. 2004; Newman et al. 2011; Richard et al. 2011), supplemented with a few other multiple images and candidates found by Zitrin et al. (2011b). In particular, we have measured, in the framework of the CLASH-VLT campaign (PI: Rosati), a redshift for system 6, identified by Zitrin et al. (2011b), to be at $z = 1.83$. However, we did not use here candidate systems 7–9 uncovered by Zitrin et al. (2011b) because these were considered somewhat less secure; we note, however, that they are easily reproducible by the models and can therefore be considered secure hereafter for future

analyses. In our LTM minimization we also leave to be freely weighted the two BCGs and the BCG ellipticity parameters, and in our PIEMDeNFW modeling we also leave the secondary BCG ellipticity free. Our WL shape measurements include 795 galaxies that lay outside the critical curves and are used for the WL constraints with an effective redshift of 1.14. In addition, we note that A383 is also one of the three CLASH clusters found to strongly magnify a background supernova (SN; Patel et al. 2014; Nordin et al. 2014), although this was not used here as a constraint.

4.3. A611

The galaxy cluster A611 ($z = 0.29$) is a well-studied, X-ray-bright but relaxed cluster, with various previous lensing analyses (e.g., Richard et al. 2010; Newman et al. 2009; Donnarumma et al. 2011, and references therein). Three secure multiple-image systems are known for this cluster, and we follow here the SL constraints (including revised redshifts) as given in Newman et al. (2013b). We also agree with their identification of additional central images for systems 1 and 3. As system 3 has no spectroscopic measurement, we leave its redshift to be optimized by the minimization procedure. We also leave the BCG to be freely weighted by the MCMC. Five hundred and forty-seven galaxies lay outside the critical curves and were used as the WL constraints, with an effective redshift of 0.86.

4.4. A1423

The galaxy cluster A1423 ($z = 0.213$) is part of CLASH's relaxed sample, and we found no record of a lensing analysis of this cluster outside the CLASH framework (e.g., Merten et al. 2014; Umetsu et al. 2014). We identify here a medium-to-small lens with a very rough Einstein radius of ~ 10–$15''$. We do not find any secure multiply imaged system but do uncover two to three candidate systems. We used one of them to construct a preliminary model using both parameterizations. This should be considered as a *crude* not well-constrained model due to the lack of multiple images. Eight hundred and four galaxies lay outside the critical curves and were used as the WL constraints, with an effective redshift of 0.92.

4.5. A2261

The galaxy cluster A2261 ($z = 0.225$) has been subject to WL analyses based on Subaru data (e.g., Umetsu et al. 2009; Okabe et al. 2010). Coe et al. (2012, see also references therein) constrained the inner mass profile of A2261, carrying out the first extensive SL analysis of this cluster using the 16-band *HST* imaging obtained as part of the CLASH program, where multiple images and candidates were uncovered with the aid of a preliminary LTM model (for another recent analysis, see also Ammons et al. 2014). We use here the more secure identifications of the Coe et al. (2012) list, as listed in Table 2, along with our WL catalog, to constrain the models.

4.6. CL J1226.9+3332

The galaxy cluster CL J1226.9+3332 at $z = 0.89$ is one of the hottest, most X-ray-luminous systems at $z > 0.6$ known to date (Maughan et al. 2007). In addition, Jee & Tyson (2009) performed a WL analysis of this cluster using *HST*/ACS images and found that this is also one of the most massive clusters known at $z > 0.6$. However, we found no record of previous SL analysis of CL 1226. In this work we find the first ~ 15 multiple images and candidates corresponding to four background objects. One

of these systems seems to be a very red giant arc prominent in the near-IR data. Our analysis also reveals a second central mass (sub) clump, requiring a second DM eNFW halo with the PIEMDeNFW parametrization.

4.7. MACS J0329.6−0211

In Zitrin et al. (2012b), we performed the first SL analysis known for the M0329 ($z = 0.45$), finding six systems of multiple images and candidates. One of the galaxies is a four-time-imaged $z \sim 6.2$ galaxy, whose properties were studied in Zitrin et al. (2012b). A spectroscopic redshift measurement for one of the systems uncovered was taken shortly thereafter, and we use it here as a constraint: system 2 is measured in the CLASH-VLT campaign to be at $z_{spec} = 2.14$, very similar to the photometric redshift estimate used in Zitrin et al. (2012b), $z \sim 2.17$.

Christensen et al. (2012) performed spectroscopic observations for the $z \sim 6.2$ galaxy, yet no secure determination of the spectroscopic redshift was achieved due to the lack of emission lines. For the minimization procedure we only use systems 1–3, which we consider as most secure, where the redshift of system 3 is left free to be optimized by the models. For the LTM model, the two brightest galaxies are left to be optimized by the model, whereas for the PIEMDeNFW model, we use two eNFW halos centered on the two brightest galaxies and leave the weight of three bright galaxies to be optimized by the model.

4.8. MACS J0416.1−2403

M0416 ($z = 0.40$) was first analyzed by Zitrin et al. (2013b) in the framework of the CLASH program, using both the LTM and PIEMDeNFW methods, and where we uncovered 70 multiple images of 23 background sources and revealed an efficient, elongated bimodal lens. M0416 was then chosen as one of the HFF targets now being observed to a much greater depth than CLASH. Zitrin supplied mass models for this cluster available online through the HFF webpage, in the framework of the HFF map-making campaign (PIs: Zitrin & Merten), in which five different groups have submitted high-end mass models for use by the community. More recently, Jauzac et al. (2014) and Diego et al. (2015b) have both published, independently, refurbished mass models for M0416, finding many additional multiple images in the supplemented HFF data, and Johnson et al. (2014) have previously published their lensing models for the HFF, including M0416 (see also Coe et al. 2014; Richard et al. 2014; Gruen et al. 2014; for other models). Grillo et al. (2014) have recently also produced a very accurate lens model for M0416, in which several redshifts from our CLASH-VLT campaign were presented. Here, we use the same set of constraints from Zitrin et al. (2013b), with a slight revision reflected in Table 2. Spectroscopic redshift for the giant arc (system 1) was available from Christensen et al. (2012).

4.9. MACS J0429.6−0253

Although M0429 ($z = 0.399$) has been subject to various X-ray studies (Schmidt & Allen 2007; Comerford & Natarajan 2007; Maughan et al. 2008; Allen et al. 2008; Mann & Ebeling 2012), we did not find any previous SL, nor WL, analyses for this cluster outside the CLASH framework. We uncover here the first two multiply imaged families: one is a multiply imaged arc with a distinctive knot in its middle, with a photometric redshift of $z_s \sim 3.9$, and the second, a four-times-imaged blob, with a photometric redshift of $z_s \sim 1.74$. Due to the very good agreement in redshift estimate among the uncontaminated

multiple images of system 2 and the dropout feature of system 1, we adopt these photometric redshifts as fixed in our modeling (also, the relative distance ratio only slightly changes for the redshifts involved). Six hundred and fifty-one galaxies lay outside the critical curves and were used as the WL constraints, with an effective redshift of 1.08.

4.10. MACS J0647.7+7015

M0647 ($z = 0.591$) is part of the 12 MACS $z > 0.5$ cluster sample (Ebeling et al. 2007), and as such was first analyzed by Zitrin et al. (2011a) in their work on this sample. Zitrin et al. (2011a) identified the first multiple images in this cluster, later revised and supplemented with additional images from CLASH data, revealing also a likely $z \sim 11$ multiply imaged galaxy (Coe et al. 2013), which is the highest-redshift galaxy candidate known to date. We used as constraints the secure identification listed in Coe et al. (2013), as seen in Table 2 here.

4.11. MACS J0717.5+3745

M0717 (0.546) is also one of the 12 MACS clusters at $z > 0.5$ (Ebeling et al. 2007), and as such was first analyzed by Zitrin et al. (2009a, 2011a) in their work on this sample. Zitrin et al. (2009a) found, using their LTM method, many multiple images in this cluster, which revealed a complex lens that constitutes the largest strong lens known to date, with an Einstein radius of $z \sim 55''$. The high lensing power of this cluster, which is a notable part of its surrounding cosmic web (Ebeling et al. 2004), qualified it as well for the HFF program, with observations planned for the near future. Other mass models for this cluster were published, both in the SL and WL regimes (e.g., Jauzac et al. 2012; Limousin et al. 2012; Diego et al. 2014; Richard et al. 2014; Johnson et al. 2014; Medezinski et al. 2013). In the latter work, we have also revised our initial multiple-image list from Zitrin et al. (2009a), following Limousin et al. (2012), with additional corrections, as listed in Table 2 here. In addition, Vanzella et al. (2014) identified two spectroscopically confirmed $z = 6.4$ lensed by M0717, which could be multiple images of the same background galaxy—as was considered in some of the works mentioned above—yet we did not use these here as constraints. Note also that in the HFF framework, we have submitted two models for this cluster, using both LTM Spline interpolation smoothing and a Gaussian smoothing, as the one we use here. Limousin et al. (2012) have shown that when modeled with analytic DM halos, this cluster cannot be well-modeled with one halo and needs five of them. For that reason, we do not use here the PIEMDeNFW parametrization, and for the current work we remodeled the cluster only in the LTM Gaussian smoothing method, with the same pipeline as for all 25 clusters (which was slightly refurbished since we made our HFF models). In this method the same simple procedure is applied to all scales, from galaxy-group lenses up to very complex clusters such as this one. Other studies of systematics in this cluster can be performed elsewhere, such as in the framework of the HFF.

4.12. MACS J0744.8+3927

As the two previous clusters in our CLASH list, M0744 ($z = 0.698$) is also part of the 12 MACS clusters at $z > 0.5$ (Ebeling et al. 2007), and as such was first analyzed in Zitrin et al. (2011a), where the first multiply imaged galaxies known for this cluster were found. We have now revised our identification using CLASH imaging and revealed several additional multiply imaged galaxies that we use as constraints; see Table 2 or
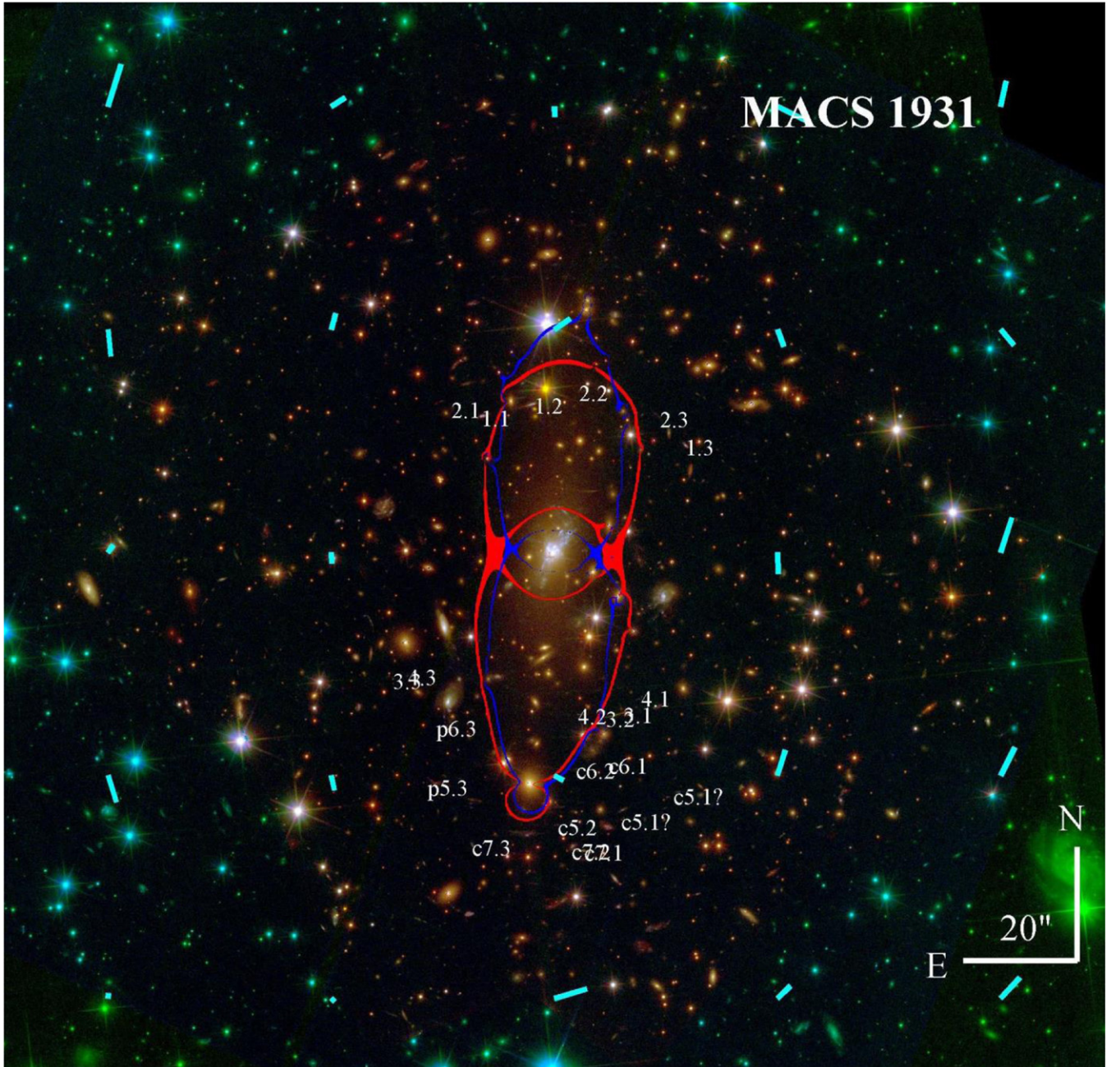
Figure 1. Multiple images and candidates (the latter are marked with "c"; "p" stands for predicted location), shear, and critical curves ($z_s = 2$), overlaid on an RGB color image constructed from the CLASH 16-band imaging, for one cluster from our sample (MACS 1931). Similar figures for the remaining 24 CLASH clusters are shown in the extended, online version of this figure. The *red* critical curves correspond to our LTM model, whereas the *blue* critical curves correspond to our PIEMDeNFW model. The measured shear, averaged here for show in $\sim [40'' \times 40'']$ pixels, is marked with *cyan* lines across the field, where the line length in each position is proportional to the shear's strength (with the overall scale factor arbitrary). Multiple images are listed in Table 2; the resulting mass profiles for this cluster are shown in Figure 2; the resulting mass–density maps are shown in Figure 3; and the differences between the various maps from the two models are shown in Figure 4.

(An extended version of this figure is available.)

Figure 1 for more details. For our PIEMDeNFW model, we use here two eNFW DM halos, as the constraints are not well explained by a single central halo. Seven hundred and forty-two galaxies lay outside the critical curves and were used as WL constraints, with an effective redshift of 1.32.

4.13. MACS J1115.9+0129

We found no record of previous lensing analyses of M1115 ($z = 0.352$) outside the CLASH framework and present here

the first SL and WL analyses in *HST* data, including the multiple images and candidates identification. In the SL regime our model includes two multiply lensed systems. The first system includes a low surface brightness giant arc and its counterimages, which was also noted and targeted spectroscopically by Christensen et al. (2012), yet no emission lines were found, and thus no unambiguous redshift could be determined. Christensen et al. (2012) have concluded a plausible redshift of either $z \sim 0.5$ or $z \sim 3.5$. For our lens models we adopt a fixed photometric

redshift of 2.84, as obtained from the BPZ program in the CLASH pipeline. The second system is a small blob imaged three times, where its images seem to follow tightly the symmetry of the lens and show similar colors and photometric redshifts. To allow for some flexibility we allowed the redshift of this system to be optimized by the minimization procedure. Our models suggest that the $z = 2.84$ redshift we adopted to system 1 may be significantly higher than its true redshift (both models suggest system 2 lies at a significantly higher lensing distance than system 1). Correspondingly, the presented models have to be treated with somewhat more caution, warranting a future revision. Four hundred and eighty-six galaxies lay outside the critical curves and were used as the WL constraints, with an effective redshift of 1.03.

4.14. MACS J1149.5+2223

M1149 ($z = 0.544$) is also one of the 12 MACS cluster sample at $z > 0.5$ (Ebeling et al. 2007) and as such was first analyzed by Zitrin & Broadhurst (2009); Zitrin et al. (2011a), where several multiply imaged galaxies were uncovered in this cluster, including a giant multiply imaged spiral (see also Smith et al. 2009) now known to host the first known multiply imaged SN (Kelly et al. 2014). With CLASH data we have now revised our multiple-image identification and revealed other multiple images (e.g., Zheng et al. 2012), which we use here as constraints; see Table 2 or Figure 1 for more details. Smith et al. (2009) found that a single DM halo does not describe well the cluster, and three more DM halos had to be added by them to obtain an accurate fit. For that reason, we do not attempt to model this cluster with the PIEMDeNFW method here and only concentrate on a new model using our LTM technique. In addition, due to its lensing capabilities, M1149 is also part of the HFF program. In that framework, we have submitted two models for this cluster, using both a Spline interpolation smoothing and a Gaussian smoothing as the one we use here. For the current work we remodeled the cluster with the exact same pipeline as for all 25 CLASH clusters (which was slightly refurbished since we made our HFF models), only in the LTM Gaussian smoothing method. Other studies of systematics in this cluster can be performed elsewhere. For additional, recent models for this cluster, see Richard et al. (2014); Johnson et al. (2014); Rau et al. (2014). In our modeling we also use, as WL constraints, 830 galaxies that lay outside the critical curves, with an effective redshift of 1.32.

4.15. MACS J1206.2−0847

M1206 ($z = 0.44$) was first analyzed by Ebeling et al. (2009) based on a prominent giant arc seen west of the BCG. Using CLASH imaging and our LTM technique, Zitrin et al. (2012c) have revealed 47 new multiple images and candidates of 12 background sources, for some of which spectroscopic redshifts were obtained in our CLASH-VLT campaign, allowing the mass profile to be constrained. Our profile was found to agree well also with an independent WL analysis by Umetsu et al. (2012) and a dynamical analysis by Biviano et al. (2013). We use here a similar set of constraints to model the cluster in both parameterizations, now also including the *HST* WL data. Five hundred and eighty-one galaxies lay outside the critical curves and were used as the WL constraints, with an effective redshift of 1.13.

4.16. MACS J1311.0−0311

We did not find a report of any SL or WL analysis for M1311 ($z = 0.494$) outside the CLASH framework. We identify here two multiply imaged systems and an additional candidate system and present the first analysis of this cluster. The first system is a dropout with photometric redshift of $z = 5.82$, and the second has a photometric redshift of 2.40. We keep these redshifts fixed throughout our minimization, while allowing the BCG's weight to be optimized, as for most of the clusters we analyzed. Four hundred forty-seven galaxies lay outside the critical curves and were used as the WL constraints, with an effective redshift of 1.03.

4.17. MACS J1423.8+2404

The galaxy cluster M1423 ($z = 0.545$) was first analyzed by Limousin et al. (2010) by SL+WL data together. Limousin et al. (2010) found and spectroscopically measured two multiply imaged systems that Zitrin et al. (2011a) later used in their analysis of the 12 $z > 0.5$ MACS clusters (see Ebeling et al. 2007). Using CLASH data, we have now found an additional multiply imaged system comprising five multiple images (system 3 here), which we use here as additional constraints. Additionally, we have found (see also Bradley et al. 2014) a few higher-redshift candidates that are possibly multiply imaged at $z \sim 6–7$ (candidate system 4 here). This option should be investigated more thoroughly in future studies.

4.18. RXJ1532.9+3021

RXJ1532, which we also refer to as MACS 1532 (Ebeling et al. 2010), contains a remarkable star-forming BCG residing in a cool-core cluster. We found no record of a previous lensing analysis prior to CLASH data. M1532 is also one of the three CLASH clusters found to strongly magnify a background SN (Patel et al. 2014; Nordin et al. 2014). The latter works have also presented models for this cluster for determining the background SN magnification; however, no multiple images were listed therein. We do not find any secure set of multiple images in this cluster and have only identified one candidate system. We correspondingly present *crude and preliminary* mass models for this cluster, while including also the WL information as constraints. Five hundred and five galaxies lay outside the critical curves and were used as the WL constraints, with an effective redshift of 1.07.

4.19. MACS J1720.2+3536

Also M1720 ($z = 0.387$) is one of the three CLASH clusters found to strongly magnify a background SN (Patel et al. 2014; Nordin et al. 2014). Nordin et al. (2014) presented a mass model (or magnification map) for this cluster, yet did not list the multiple images used as constraints. Patel et al. (2014) also presented a model based on WL data and on the list of multiple images we have now identified and list here for the first time (Table 2).

4.20. MACS J1931.8−2635

We did not find any record of a previous lensing analysis for M1931 ($z = 0.352$) outside the CLASH framework. We identified 22 new multiple images and candidates of seven background sources, which we use as SL constraints on top of our WL shape measurements, revealing a remarkably elongated lens. Seven hundred and eight galaxies lay outside the critical

curves and were used as the WL constraints, with an effective redshift of 0.82.

4.21. MACS J2129.4−0741

M2129 ($z = 0.59$), like several other clusters mentioned above, is also one of the 12 MACS clusters at $z > 0.5$ (Ebeling et al. 2007) and as such was first analyzed in Zitrin et al. (2011a), where the first multiple images in this cluster were uncovered. Here, we supplement this identification with additional multiple images now uncovered in CLASH data and use these to constrain the cluster lens model, in conjunction with the WL data. Eight hundred and fifty-one galaxies lay outside the critical curves and were used as the WL constraints, with an effective redshift of 1.23.

4.22. MS 2137-2353

MS2137 ($z = 0.313$) seems to be a well-relaxed cluster and exhibits a giant arc. Several attempts to model the mass in cluster took place, albeit with some tension between the results (e.g., Gavazzi et al. 2003; Sand et al. 2008; Donnarumma et al. 2009; Newman et al. 2013b, and references therein). The tension mainly arises from different mass profile estimates and is due to lack of enough multiple images to properly constrain the slope of this cluster: only two multiply imaged galaxies were known before, the aforementioned giant arc and an additional system, both at a similar redshift of $z_s = 1.5$ (Donnarumma et al. 2009, and references therein). Because the mass profile is coupled to the lensing distance ratio between different-redshift multiply lensed galaxies, it was essentially impossible to place strong constraints on the inner mass profile of this cluster from lensing alone. Using our LTM method we were now able to identify three images of an additional multiply lensed galaxy, verified by the CLASH *HST* imaging and Very Large Telescope (VLT) spectroscopy from the CLASH-VLT run (PI: P. Rosati), which allows the inner mass profile of this cluster to be reliably constrained (because the latter system has a different, and substantially higher, redshift than the first two systems, $z_s = 3.09$). Seven hundred and eighty-five galaxies lay outside the critical curves and were used as the WL constraints, with an effective redshift of 1.12.

4.23. RXJ1347.5−1145

RXJ1347 ($z = 0.45$) is one of the most X-ray-luminous clusters known (e.g., Schindler et al. 1995, as one example), and as such was the subject of several lensing analyses (Halkola et al. 2008; Bradač et al. 2008; Köhlinger & Schmidt 2014). Using our LTM method we chose the most reliable identification of multiple images from these previous lensing works, listed in Table 2, as constraints for our model, along with the *HST* WL data. Six hundred and thirty-three galaxies lay outside the critical curves and were used as the WL constraints, with an effective redshift of 1.13.

4.24. RXJ2129.7+0005

RXJ2129 ($z = 0.234$) was previously studied in the framework of the LoCuSS collaboration: A WL analysis was published, for example by Okabe et al. (2010), and a SL analysis was published by Richard et al. (2010), based on one identified system. The redshift of this system was published by Richard et al. (2010) to be $z_s = 1.965$. Recently, Belli et al. (2013) revised the (spectroscopic) redshift measurement to $z = 1.522$, which is the redshift we adopted for our analysis. In addition,
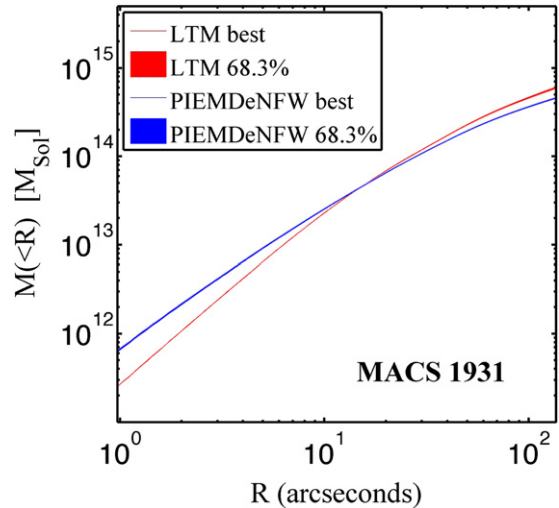

Figure 2. Resulting 2D-integrated mass profile as a function of radius for an example cluster from our sample (MACS 1931; seen in Figure 1), from both the LTM and PIEMDeNFW models (see Section 3). Similarly, profiles for all other 24 CLASH clusters are shown in Figure 9.

we publish here five new sets of multiple images and candidates, whose redshifts we left to be optimized by the minimization procedure. These allow us to put much stronger constraints, for the first time, on this cluster's mass distribution and profile.

4.25. RXC J2248.7-4431

RXJ2248 ($z = 0.348$), also known as A1063S, was recently analyzed for the first time by CLASH (Monna et al. 2014, see also Balestra et al. 2013; Gruen et al. 2013), uncovering many multiple images, including a $z \sim 6$ galaxy imaged five times. We use these constraints as listed in Table 2 for the SL part, jointly with the *HST* WL shape measurements. Note also that we have already published mass models for this cluster (SL only) in the framework of our HFF map-making group (PIs: Zitrin & Merten) available online, yet here we rerun those models with the slight modifications to our code to be coherently analyzed as all other clusters in our sample. Additionally, other mass models from other HFF lens modelers are available online through the HFF page (e.g., Johnson et al. 2014; Richard et al. 2014).

5. RESULTS AND DISCUSSION

We constructed lens models for the full CLASH cluster sample, using both the SL and WL signals, in deep *HST* observations taken in the CLASH program. For most clusters, we used *two distinct* common parameterizations: the full LTM parameterization, assuming LTM for both galaxies *and* the DM, and a parametrization in which LTM is only assumed for the galaxies, while the DM is modeled separately and analytically with an eNFW halo (or two, for more complex merging clusters). Our main goal was to present here the mass models and the multiple-image catalogs and to release them to the community along with an investigation of the typical, systematic differences.

In Figure 1 we plot the critical curves for one example cluster from the two parameterizations, on an RGB image constructed using the 16-band CLASH observations. In Figure 2 we plot the resulting 2D integrated mass profiles (see Figure 9 for the profiles of the full sample). Figure 3 shows the dimensionless mass-density distributions κ for both the LTM and PIEMD+eNFW

models. The differences in κ and magnification between the two models, relative to the LTM model (which we arbitrarily chose as our reference model), are seen in Figure 4, and their histograms gathered from all clusters are shown in Figure 5. Note that similar plots to those included in Figures, 1, 3, and 4, *for all clusters*, are included in the extended, online version of these figures. In Figure 6 we stack the relative systematic differences in the magnification, surface density, and shear, as a function of the radius from the cluster center and as a function of the respective best-fit values of these quantities. Note that the ordering of the clusters in the figures may slightly differ from the order in Section 4.

5.1. Systematics and Statistical Uncertainties

We discuss the statistical and systematic uncertainties probed by our analysis with two distinct mass-modeling parameterizations.

5.1.1. Magnification and Mass–Density Maps

As is evident from Figure 1 (see full version online) the critical curves from both parameterizations (where available), for each cluster, are in overall good agreement. Despite the quite distinct parameterizations, this may not be too surprising, as in practice similar multiple-image constraints are used for both solutions, directly determining where the critical curves should pass for each multiply imaged system. This is also why it is important to compare the resulting maps to one another, in order to see what are the differences both in the SL regime and across the larger FOV where the constraints from SL are poor or nonexistent.

We wish to provide a reasonable estimate of how strongly the choice of parameterization affects the resulting maps of mass density, κ, and magnification, μ. Such an estimate of the underlying systematics is crucial for any work which relies on the lens models for their study, such as measurements of the actual lensed volumes, properties of lensed galaxies, or the intrinsic properties of magnified, high-redshift background objects, especially in the current epoch of increasing interest in magnified,

high-redshift galaxies and with recent, extensive cluster-lensing surveys using *HST* such as LoCuSS (PI: G. Smith; e.g.,Richard et al. 2010), CLASH (Postman et al. 2012), and the ongoing HFF (Lotz et al. 2014). For each cluster, for the κ and μ maps separately, we subtract each map from the corresponding map in the other parametrization and divide the absolute value of the result by the LTM map, as a reference, to obtain relative residual maps. These are seen for one example cluster in Figure 4 here—and for the other 24 clusters—in the extended, online version of this figure, respectively. For each cluster we also note therein the median, mean, and 1σ dispersion of each map.

Regarding the magnification differences, a few things are evident from Figure 4 (see full version online). First, it is clear that most of the relative systematic differences are seen next to the critical curves, where the magnification diverges. Second, as a result, the median and mean differ significantly in most cases, and the standard deviation is huge. This is not surprising, as these are governed by the error induced by the diverging critical curves. In Figure 5, we make a histogram of both the absolute and the relative difference in the magnification, gathered from all pixels across the 23 clusters that were analyzed with the two methods. The 68.3% C.L. of the relative magnification differences is [0.08, 0.44], with a median(mean) of 0.22(0.27), implying a typical $\sim$20% systematic error relative to the reference LTM model, on the magnification across the probed, central $\sim$ [$4\rlap{.}'6 \times 4\rlap{.}'6$] FOV. In terms of absolute magnification differences, the 68.3% C.L. in $\Delta\mu$ is [0.11, 1.12], with a median(mean) of 0.37(0.65).

Interesting information is also gained by looking at the *kappa* map relative differences. As seen from Figure 4 (see full version online), the typical *kappa* relative differences are much larger than those in the magnification. This may be surprising at a first glance, as we know that the magnification varies more rapidly than *kappa* and is more susceptible to small changes in *kappa* (recall that $\mu = 1/((1-\kappa)^2 - \gamma^2)$). However, since each multiple-image system supplies direct constraints on the position of the critical curves, yet only constrains the total mass
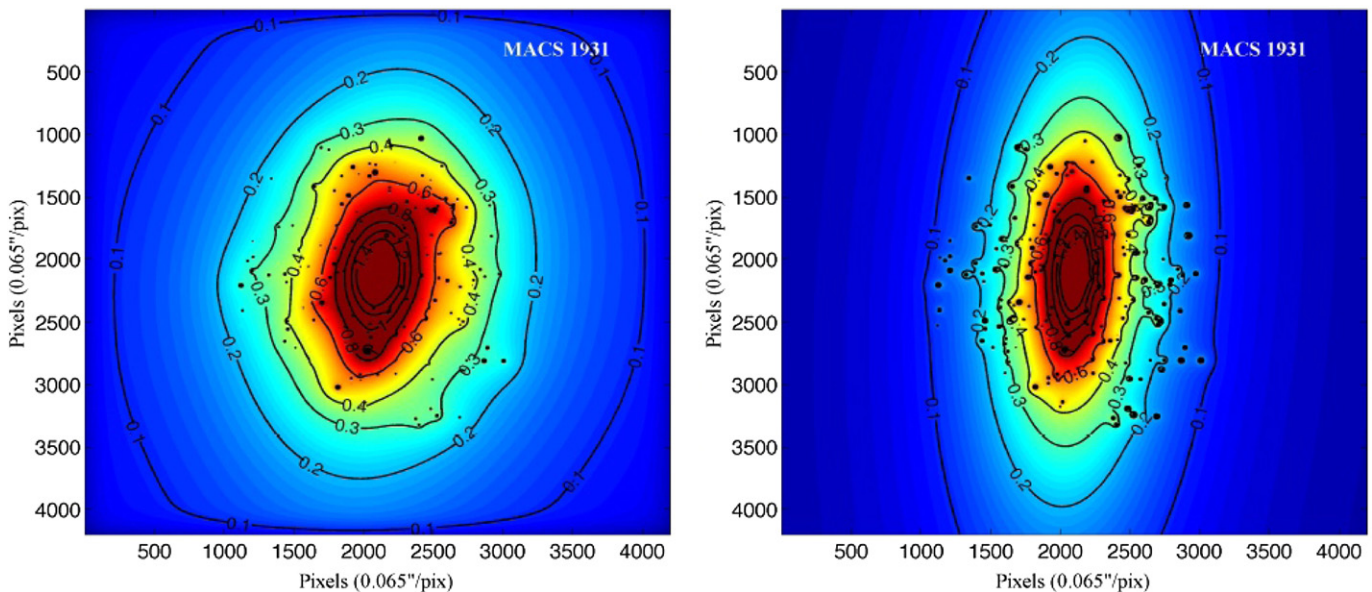

Figure 3. Projected surface mass density (κ) map from our LTM (left) and PIEMDeNFW (right) models for MACS 1931. Note the difference in ellipticity despite the similarity of the critical curves seen in Figure 1. For similar maps of all other 24 CLASH clusters, see the online, extended version of this figure. These κ maps are scaled to a fiducial redshift corresponding to $d_{ls}/d_s = 1$, as was adopted for the CLASH and HFF mass model releases online.

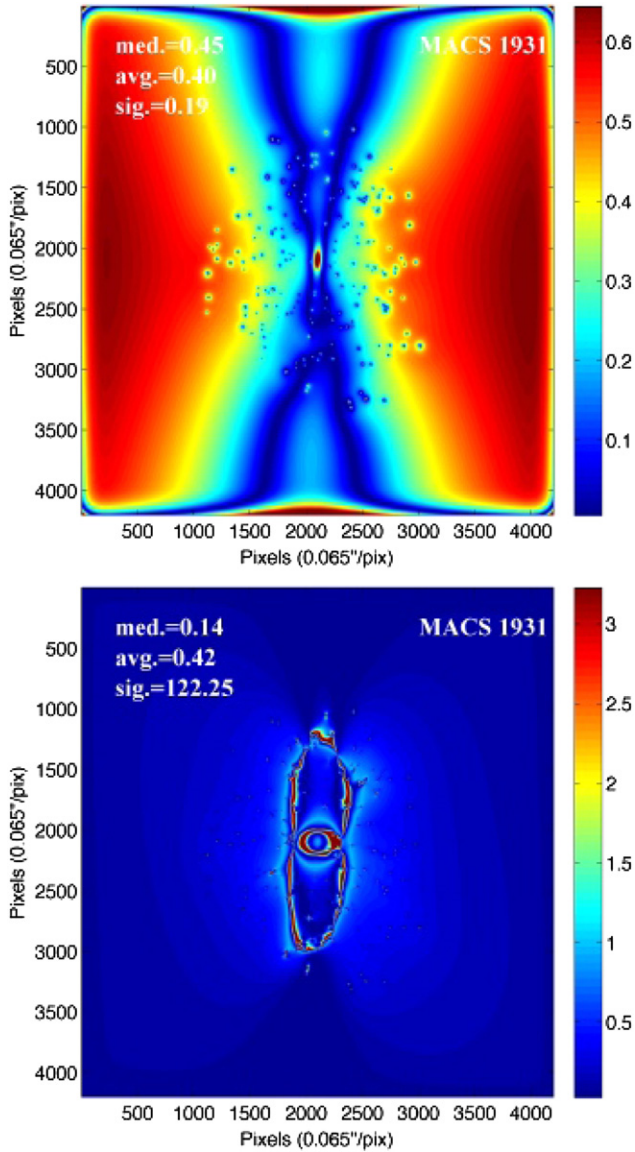(An extended version of this figure is available.)

11

Figure 4. Upper panel: absolute value of the difference between the LTM κ map and the PIEMDeNFW κ map for MACS 1931, seen in Figure 3, relative to the LTM map, which we take as a reference. On the figure we note the average, median, and standard deviation values. As can be seen, differences are mainly caused by ellipticities being assigned to the PIEMDeNFW mass–density distributions directly, while the LTM mass–density distribution simply follows the light and no ellipticity is introduced to it directly (albeit some ellipticity is incorporated in the BCG). Additionally, artifacts from the smoothing procedure introduce squareness in the LTM models near the edges of the FOV, contributing further to the discrepancy near the edges (this will be overcome in future analysis). A similar map for the other 24 CLASH clusters is available in the extended, online version of this figure. We find that the typical (*median*) difference in κ throughout this FOV among the CLASH sample is ∼40%, and the distribution of differences of all examined clusters is shown in Figure 5. See also Section 5 for more details. Lower panel: same as the Upper panel, but now showing the absolute value differences in magnification, relative to the LTM model. The majority of differences arise from the diverging critical curves and their surroundings, whereas farther away from them the error decreases. A similar map for all other CLASH clusters is available in the extended, online version of this figure. We find that the typical difference in μ, throughout this FOV among our sample, is ∼20%, and the distribution of differences is shown in Figure 5. See Section 5 for more details.
(An extended version of this figure is available.)

within those critical curves, the constraints on the distribution of the magnification are, in a way, more direct than those on kappa. More importantly, while in the PIEMD+eNFW parametrization the ellipticity is embedded directly into the mass distribution, in the LTM case there is no ellipticity assigned to the mass distribution (although some ellipticity is embedded in the BCG); the overall ellipticity, other than that induced by the BCG, only enters in the form of an external shear that has an effect on the magnification map or critical curve's ellipticity (and on the shear map), yet it does not affect the mass distribution itself, which is coupled to the light. This often creates a prominent discrepancy between the mass–density distributions resulting from these two parameterizations: because lensing only constrains combinations of κ and γ, it is possible to reproduce similar critical curves (or magnification maps and, to some extent, reduced shear maps) from these two different parameterizations that have distinct κ maps, and the degeneracy between them is not broken with typical SL+WL lensing constraints alone. In that sense, in Figure 6, we show stacked plots of the typical difference in magnification, mass density, shear and reduced shear, as a function of radius from the center and as a function of the best-fit values of these quantities. Among other interesting trends, this figure shows that while the different assignment of ellipticity in the two methods may create a prominent difference in the *kappa* maps, it does not affect the shear—that can be similar whether it stems from the mass-distribution ellipticity or is directly the external shear—to a distinguishable extent. In other words, even the combination of SL and WL does not seem to be enough to distinguish between a model in which all the lensing signal is attributed to an intrinsically elliptical lensing cluster, and a model in which no overall ellipticity is input into the mass distribution and is only imitated by adding an external shear (see also Bartelmann 1995). This degeneracy might be broken, in principle, using these lensing constraints together with additional, independent, and direct constraints on the magnifications (e.g., such as lensed supernovae Ia; albeit, these are rare) or relative magnifications between multiple images of the same source. One possibility to further examine this would be to construct a model that allows both for intrinsic ellipticity *and* external shear, to better characterize the degeneracy between them and see what their relative contributions are on an ensemble of clusters. Additionally, a comparison to numerical simulations may shed some light on the true underlying mass distribution of such clusters. It will be worth pursuing such paths in the near future.

Another minor contribution to the systematic differences in *kappa* comes from a numerical artifact in the LTM method that induces squareness into the *kappa* map close to the edges of the FOV, due to imperfect (or aperiodicity in the) boundary conditions for the Fourier transform used in our smoothing procedure (significantly speeding up the calculation). This is seen clearly in the patterns shown in Figures 14 and 16 and can be overcome in the future by refining the boundary conditions or by simply taking a larger mock FOV to then be cut to the desired size while getting rid of the affected corners of the larger FOV (such a solution would be too time-consuming, however, to be performed on the 25 cluster sample in a reasonable time frame for this work). In fact, we note that very recently we have managed to overcome this artifact and now produce "cleaner" maps without affecting the speed of the calculation much. This, however, will only be implemented and better tested in future analyses. This artifact contribution here, however, seems to be very minor in most of the field compared to the intrinsic differences between the two parameterizations and contributes significantly only very close to the edges (see, e.g., Section 5.1.3).

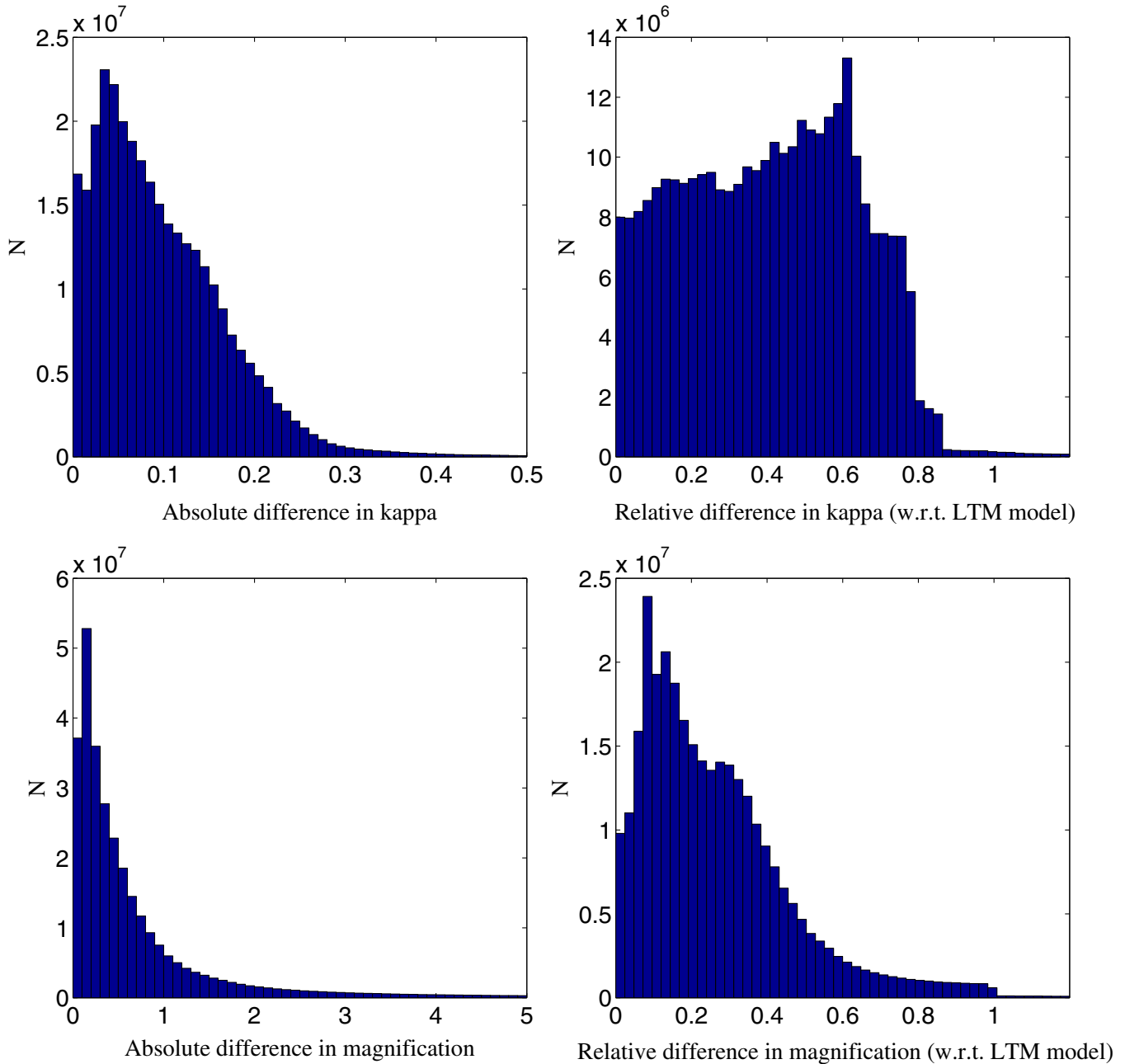We show histograms of both the absolute and relative differences in κ in Figure 5. The 68.3% C.L. of the relative κ

Figure 5. Histograms of the absolute (left) and relative (right) differences in the surface mass density κ (upper panel) and the magnification μ (lower panel) between the two methods we employed here, reflecting the systematics differences between them. For details, see Section 5.1.1.

differences is [0.14, 0.65], with a median (mean) of 0.42 (0.41), implying a typical ∼40% relative systematic error. In terms of absolute kappa differences, the 68.3% C.L. in $\Delta\kappa$ is [0.03, 0.17], with a median (mean) of 0.08 (0.10). This typical, relative difference we find (∼40%) constitutes a significant systematic error, arising mainly from degeneracies inherent to lensing as aforementioned (embedded in the two different parameterizations). Although most lensing-related studies are more dependent on the magnification estimate or the overall mass-distribution properties than on the value of each point in the *kappa* map, so that these errors may have less affect on related science, it is important to be aware of them.

Because the lens models are constrained using multiply imaged sources at different redshifts, this places immediate constraints on the resulting mass profile, so that one expects smaller differences in the averaged *kappa* or enclosed mass

profile (which is of course also relevant for related studies, such as structure formation, the concentration–mass relation, etc.), especially within the SL regime or critical curves. We probed the resulting enclosed masses and integrated mass profiles in Section 5.1.2 and 5.1.3 below.

Last, we note that the values mentioned above, extracted for the histograms of relative differences in the magnification and surface density, remain effectively unchanged whether we probe the [4′.6 × 4′.6] FOV or an inner [4′ × 4′] FOV, showing that the effect of the boundary artifact discussed above on the overall differences is very minor.

The examination of systematics in lens modeling has been a long-standing crucial task, especially in recent years where advanced modeling techniques have been developed and *HST* space imaging has allowed increasingly accurate lensing analyses and studies of high-redshift magnified galaxies. To our
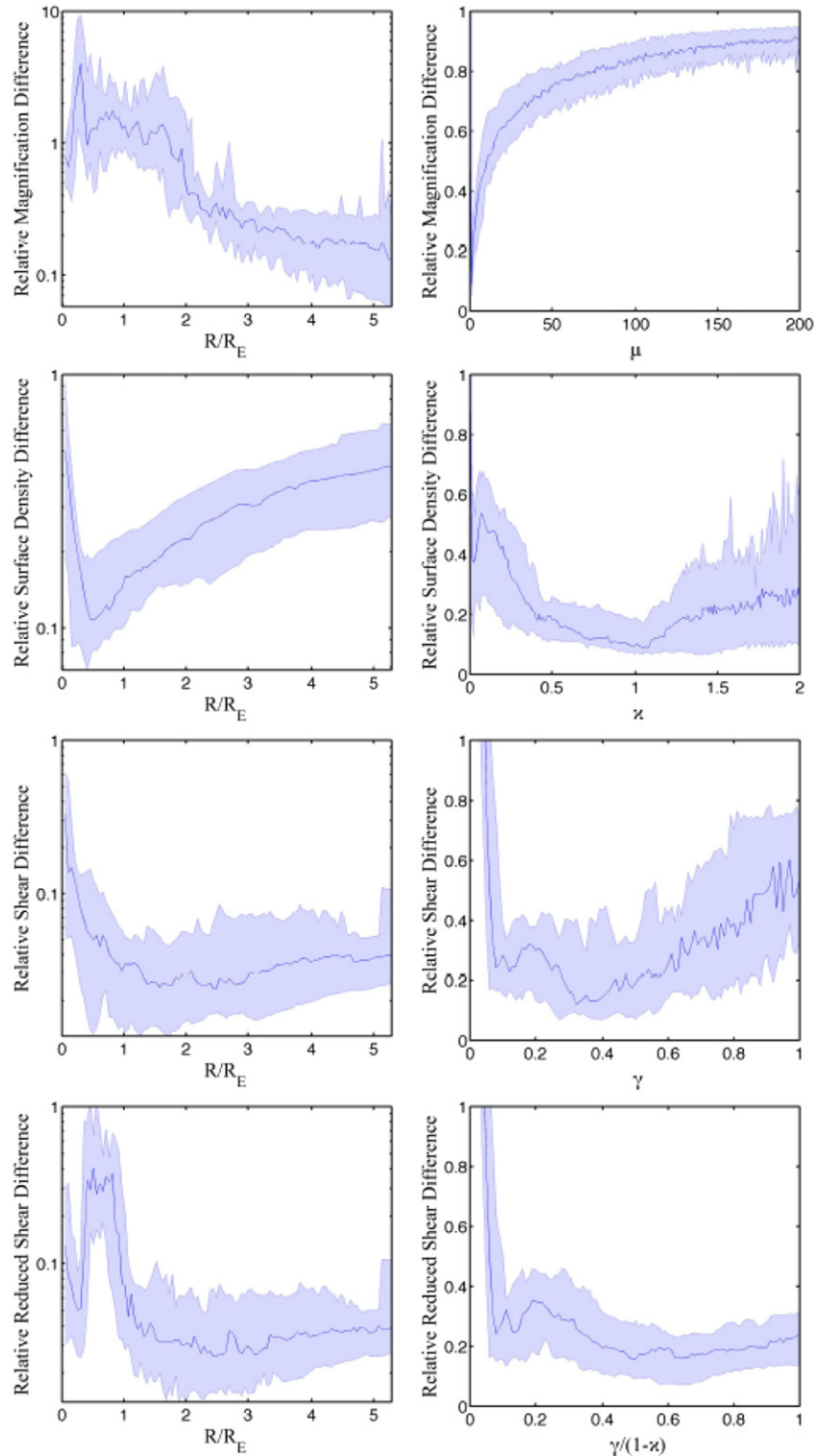
Figure 6. Systematic differences, relative to the LTM model, of the magnification (top row), surface density (second row), shear (third row), and reduced shear (bottom row), as a function of the radius from the center, in units of Einstein radius (left), and as a function of the respective best-fit values of these quantities (right). The plots are obtained by (median-) stacking the 23 clusters that have models in both parameterizations, and the shaded area represents the 1σ confidence limit (following the scatter in each bin). The top row shows that the radially averaged, systematic magnification difference decreases with radius from the center and that this difference increases rapidly with magnification value so that larger magnifications have larger relative errors. The second row shows that the radially averaged surface density difference, as expected, is minimal, at about half the Einstein radius, where kappa is close to unity. The third row shows that the mean difference in the bin-averaged shear as a function of radius is roughly constant throughout most of the range and is significantly smaller than the error on kappa (although it can be higher for shear values close to zero or one). This is an important point: the major factor causing differences between the two models is the overall ellipticity that is being in one case assigned directly to the mass distribution and in the other case implemented as an external shear not affecting the mass-distribution shape. This may create a prominent difference in the kappa maps, yet does not affect the shear (that can be similar whether it stems from the mass-distribution ellipticity or is directly the external shear) to a distinguishable extent. The bottom row shows, for completeness, the radially averaged differences in the reduced shear. Here the behavior is similar to that of the shear, with a "bump" where kappa is roughly unity, boosting the reduced shear. Overall, it is evident from these figures and from our analysis that the two parameterizations cannot be easily distinguished with the strong and weak lensing data used. Additional information, e.g., on the magnification, might come in handy to break this inherent degeneracy in the origin of ellipticity.

knowledge, our results constitute the first time such a systematic uncertainty estimate is performed over a meaningful sample of well-analyzed clusters, with two different common techniques. Other comparisons were made for single clusters in past studies (e.g., Zitrin et al. 2010; Coe et al. 2012). Our insight on the systematics can be regarded as an introduction to systematics in the HFF program in which six clusters were modeled, using various different parameterizations or techniques, by five different lens-modeling groups to assess the underlying systematic differences (see for example Coe et al. 2014). These will also be tested on simulated clusters. In that case, more modeling methods will be used to assess the underlying systematics compared to our work here, but on a much smaller sample of clusters. Both tests are of course important to perform.

5.1.2. Einstein Radius and Einstein Mass Distributions

The effective Einstein radii and enclosed masses for a fiducial redshift of $z_s = 2$ are summarized in Table 1. Note that here we measured the effective Einstein radii numerically by summing all pixels enclosed within the tangential critical curves according to the magnification sign and including also the area within the radial critical curves, where the sign of magnification flips again, to derive the critical area, A, where $\theta_e = \sqrt{A/\pi}$. The measured Einstein radii of the sample clusters, from the two distinct analyses, agree within ~10%, where the enclosed masses agree typically within ~15% (but with some outliers). This is a good agreement that is not surprising: each multiply imaged system directly places strong constraints on the Einstein radius for its redshift, and thus the enclosed mass (the mass enclosed within the Einstein radius, e.g., for a circularly symmetric lens, is proportional to the Einstein radius squared, $M_e \propto \theta_e^2$). We therefore adopt these values, i.e., ~10% and ~15%, as the representative systematic uncertainties on the Einstein radius and enclosed mass, respectively.

5.1.3. Mass Profiles

In Figures 2 and 9 we show the resulting 2D-integrated mass profiles of the CLASH sample from our two modeling methods. The main difference between the two profiles is in each method's prescription: the PIEMDeNFW fit, governed by the analytic DM form, is bound to be well-behaved and show a profile following, roughly, the input analytic (NFW in our case) form; while the LTM fit is not coupled to any analytic form, and although the mass *distribution* is coupled to the light distribution, the *profile* is in practice more flexible than the first method, in the sense that it does not follow a certain predetermined form, thus probing a wider range of profile shapes. We test the discrepancy in the total 2D-integrated mass between the two methods, $M_{2D}(< \theta \simeq 136'')$. We find a typical (median) 38% difference between the two values over all relevant clusters (see Table 1). In terms of *relative* error on the enclosed mass, compared to the LTM reference set of models, we find that the median relative error on enclosed masses, M_{2D} $(< \theta \simeq 136'')$, is ~28%. To examine how much the squareness-artifact (Section 5.1.1) may affect the discrepancies, we also examine the same difference as above inside the "artifact-free" region ($\lesssim 120''$), finding that the median, relative systematic difference in $M_{2D}(< \theta \simeq 120'')$ between the two models is somewhat smaller, with a median of ~25%, implying that most of the discrepancy originates from the different parameterization and that the boundary artifact in the LTM model contributes only about ~10–20% to the discrepancy, near the edges. In that respect, we recommend using the current LTM models up to 2
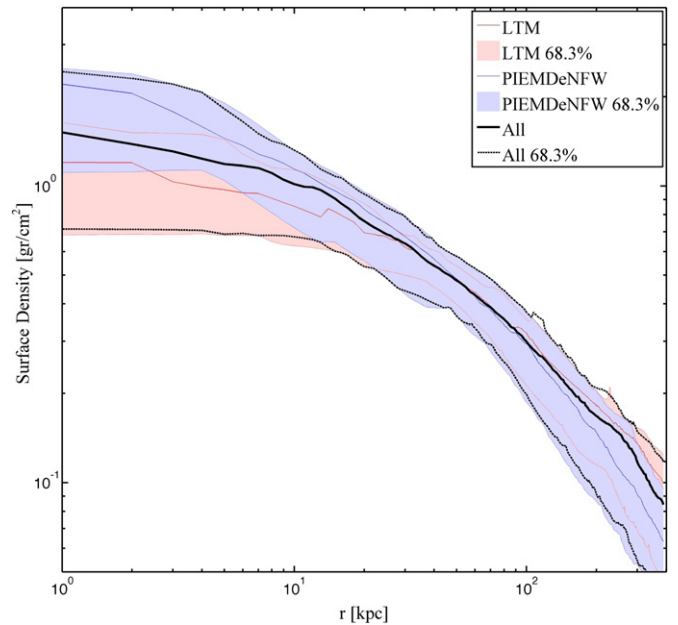

Figure 7. Stacked mass–density profile. The plot shows the projected, radially averaged mass density in g/cm² as a function of radius from the center in physical units (kpc), averaged over the 23 clusters that were modeled with both parameterizations. The *red* plot shows the stacked LTM profile, the *blue* plot shows the stacked PIEMDeNFW profile, and the *black* lines represent the combined stacked profile and 68.3% confidence intervals. As can be seen, the LTM profile is systematically shallower than the PIEMDeNFW profile. For more details, see Section 5.1.3.

arcmin in radius (however, we checked that concentrating only on the inner [4' × 4'] does not change the statistical results, or differences between the two methods, obtained here from the full [4.'6 × 4.'6] FOV).

Figure 9 also reveals that the LTM method generally yields a shallower outer mass profile (and thus a higher enclosed mass) than the PIEMDeNFW model. In Figure 7 we plot the stacked (i.e., averaged in radial physical bins over the 23 clusters) mass–density profile from both methods. Despite evident disagreement in the mass profiles of each individual cluster (e.g., Figure 9) between the two methods, the two *stacked* profiles from the two methods usually agree within the 68.3% confidence intervals, deduced by the scatter in each bin of the 23 profiles. For the PIEMDeNFW model we measure a decline in surface mass density (Σ, in (g cm^{-2})) with physical radius, r (kpc), of $d \log(\Sigma)/d \log(r) = -0.71$, in the radial range [5,350] kpc, and for the LTM model we measure a decline of $d \log(\Sigma)/d \log(r) = -0.57$ in the same range, in excellent agreement with previous LTM analyses of well-studied clusters (e.g., Broadhurst et al. 2005; Zitrin et al. 2009b). For the combined sample from the two methods together, we correspondingly obtain a slope of $d \log(\Sigma)/d \log(r) = -0.64$ in that range, whereas the errors on these slopes are roughly ±0.1.

5.1.4. Statistical Uncertainties: Call for Caution

The statistical uncertainties are naturally coupled to the σ errors plugged into the χ^2: σ_{pos}, the positional uncertainty in multiple images' location, and σ_{ell}, the WL shape measurement uncertainty. Smaller σ values will generally entail smaller statistical uncertainties. Here, we adopted sigma values following recent works, most notably that of Newman et al. (2013b) who investigated which SL positional uncertainty is preferable to consistently combine the SL constraints with WL shape measurements, whose error is generally well known ($\sigma_{\text{ell}} \sim 0.3$).

They found that a value of $\sigma_{\mathrm{pos}} = 0\rlap{.}''5$ works best, e.g., with respect to the Bayesian evidence as a criterion. This value is indeed often used in SL analyses.

As Newman et al. (2013b) also mention, however, this value of $0\rlap{.}''5$ does not account for the contribution of foreground or background structure (e.g., large-scale structure; LSS) along the line of sight, or other complex substructures in/near the cluster itself which may have been disregarded in the modeling. Similarly, in our previous SL analyses, we therefore usually used a SL sigma value of $\sigma_{\mathrm{pos}} = 1\rlap{.}''4$, which we have found takes into account modeling uncertainties arising from, e.g., contribution of LSS (e.g., Jullo et al. 2010; D'Aloisio & Natarajan 2011; Host 2012). This cosmic noise has a noticeable impact on deep SL observations in the cluster core, where magnified sources lie at greater distances (Umetsu et al. 2011b), so that it has to be taken into account especially when deep *HST* observations are combined with, e.g., shallower ground-based WL observations. This conservative error of $\sigma_{\mathrm{pos}} = 1\rlap{.}''4$ was indeed found to be more realistic when the SL mass profile is combined with outer WL measurements from Subaru observations (Umetsu et al. 2012). When accounting for possible systematic uncertainties due to prior assumptions inherent to SL modeling, we found even larger errors for $M_{2D}(< \theta)$ from SL (see Section 4.3 of Umetsu et al. 2012 for their regularization technique), which resulted in a $\sim20\%$ uncertainty on the total projected mass enclosed within the effective Einstein radius. This is consistent with our representative systematic uncertainty on the Einstein mass estimate ($\sim15\%$).

We therefore conclude that statistical errors arising from a choice of σ_{pos} of $0\rlap{.}''5$ are likely much underestimated (i.e., they neglect the governing systematic errors). Hence, we apply here nominal, minimum errors on various quantities. For example, we a priori adopted throughout 10% and 15% nominal errors on the Einstein radius and mass, based on our previous analyses (e.g., Zitrin et al. 2012c), overriding the "official" statistical 1σ errors by an order of magnitude. Not surprisingly, these are also similar to the *systematic* errors we find here for these quantities, between the two modeling methods. These minimal errors are important not to underestimate the true errors and also because our models and *statistical* error maps are made publicly available online and may be used in future studies. While it may be relatively easy to rescale errors resulting from a one-term χ^2 to any desired σ value, it may not be trivial for a two-term χ^2, such as for a SL+WL combined analysis. For this reason, we chose one cluster and reran our complete analysis with $\sigma_{\mathrm{pos}} = 1\rlap{.}''4$. While this somewhat underweights the SL constraints relative to the WL constraints, it will teach us by how much the typical errors increase. We find that errors on the integrated mass profile are $\sim40\%$ larger per bin, on average, when using the more realistic $\sigma_{\mathrm{pos}} = 1\rlap{.}''4$ than the errors when using $\sigma_{\mathrm{pos}} = 0\rlap{.}''5$.

We therefore recommend that for future studies the statistical errors arising from our present analysis (i.e., with $\sigma_{\mathrm{pos}} = 0\rlap{.}''5$) be replaced with the actual and much larger systematic uncertainties we find in this work, to represent more realistically the true underlying (statistical+systematic) errors. These are summarized in the Abstract and in Section 6.

5.2. Quality of Fit and Comparison of the Two Methods

When modeling a sample of clusters with two distinct parameterizations, a natural question arises: is there a statistically preferable parameterization? From our analysis we cannot unambiguously, strongly prefer one parameterization over the other, and the current study mainly sharpens the differences between them and thus the advantages and disadvantages of each method (for previous examination of the differences between these parametrizations, see, e.g., Zitrin et al. 2013b).

Statistically, the PIEMDeNFW model seems to yield usually a more *accurate* and well-behaved result. This is reflected, for example, in the rms, reduced χ^2, or Bayesian evidence, which are often (in 16 out of the 23 modeled clusters analyzed with the two methods) better for the PIEMDeNFW parameterizations, suggesting it is statistically preferable in most cases. For example, the natural logarithm of the Bayesian evidence (Table 1) is, on average, typically larger by a few dozens for the PIEMDeNFW models in these 16 cases for which the fit is better than that of the LTM. However, recall that in Section 5.1.4 we emphasized that the statistical errors here are strongly underestimated because of the choice of σ for the χ^2 terms. Replacing, for example, the positional uncertainty with the more realistic value of $1\rlap{.}''4$, the Bayesian factor comparing the two methods should become less significant—typically, the expected difference will be a factor of ~8 smaller—though still mildly preferring the PIEMDeNFW model.

Additionally, note that if the PIEMDeNFW model is often somewhat more *accurate* in terms of rms, we regard the LTM parametrization as often more *reliable* (at least as a first-guess simple solution) because it relies on a very simple assumption entailing a remarkable predictive power to find many multiple images, even when the fit is obtained by "just following the light," without any initial multiple-image constraint as input (e.g., Broadhurst et al. 2005; Zitrin et al. 2009b, 2012a) and because it is not coupled to a certain analytic form and thus allows for a more flexible profile shape (it is only coupled to the light distribution). Recall that on the far end of the "accuracy" scale lies nonparametric modeling (e.g., Abdelsalam et al. 1998; Diego et al. 2005; Liesenborgs et al. 2006; Coe et al. 2008), in which the solution is approximately perfect in terms of multiple-image location reproduction rms. In such methods, typically, no prior assumptions are applied to the mass distribution and the result is directly inferred from the set of constraints; however, the typical low number of constraints relative to the FOV or grid size results usually in a very low-resolution solution, with hardly any predictive power to find additional multiple images. Therefore it is clear that *accuracy* does not necessarily mean *reliability*. Additionally, besides its immense predictive power, the fact that the same simple LTM procedure reasonably fits any lens from galaxy-scale lenses, through galaxy groups and relaxed clusters, and up to highly complex clusters, without a need to add additional DM clumps, such as in the PIEMDeNFW parametrization, adds even more to its assumption reliability. On the other hand, as the LTM mass distribution is strongly coupled to the light distribution, bright galaxies that are not necessarily as massive as their luminosity indicates (or vice versa), meaning galaxies that deviate strongly from the effective M/L ratio adopted, can strongly affect or bias the result. In such cases a good eye for lensing and a user intervention is needed, more significantly than in the analytic PIEMDeNFW. Such bright galaxies, if included, can artificially boost the critical curves, which may have led to an overestimation of the Einstein radius sizes in previous works (e.g., for two to three clusters in Zitrin et al. (2011a), but based on poorer *HST* data—prior to CLASH imaging).

To summarize, it seems that in most cases the analytic, PIEMDeNFW model supplies more accurate results and therefore is

likely preferable for "final," precise lens models, while the LTM advantages are its simplicity and initial predictive power, which can be used, for example, to find many sets of multiple images for new clusters. We conclude, therefore, that both are equally valuable and useful, each for its own advantages, which is why it was interesting to test the systematic differences between them and why it is important to model clusters with more than one method (such as in the HFF program), for a better grasp of the systematics.

5.3. Mass-sheet Degeneracy?

The mass-sheet degeneracy—or, more generally—transformation (MST hereafter), is a fundamental degeneracy in lens modeling (Falco et al. 1985; Liesenborgs & De Rijcke 2012; Schneider & Sluse 2013). Because we use parametric modeling, coupled with usually at least two measured/fixed redshifts for multiple objects in each cluster, the MST is expected to be readily broken, and thus the differences that we see between the models should not be attributed to MST (also, MST does not alter the isocontour shape or of the mass distributions, which, as we saw, is the main cause of difference here originating from the difference in ellipticity assignment). It is, however, interesting to test this assumption. For that purpose, for each field we calculated (in the "artifact-free" area, $\theta < 120''$), the value of λ, the constant in the MST, given by $\lambda = \sum_i (\kappa_{i,\mathrm{LTM}}(\kappa_{i,\mathrm{NFW}} - 1))/\sum_i (\kappa_{i,\mathrm{LTM}}(\kappa_{i,\mathrm{LTM}} - 1))$. The MST would then be $\kappa_{\mathrm{LTM}} \to \kappa_{\mathrm{LTM}}\lambda + (1 - \lambda)$, and $\gamma_{\mathrm{LTM}} \to \gamma_{\mathrm{LTM}}\lambda$ (where γ_{LTM} refers to the intrinsic shear in the LTM models, i.e., neglecting the external shear). We repeated this calculation and transformation for each LTM map of the 23 clusters that was analyzed with the two methods and repeated the tests for the systematic differences we described in this work, now between the PIEMDeNFW maps and the MST-corrected LTM maps. If the MST really accounts for the differences between the two mass models, the differences should vanish. From this investigation, we reach the following conclusions:

1. Accounting for MST reduced the typical relative differences in the κ maps from $\sim$40% to $\sim$30%—so that major differences still remain. MST therefore cannot account for the differences between the mass maps.

2. If the MST could account for the differences between the mass maps, we should see a (at least roughly) constant λ value across the FOV for each cluster. In contrast, we get that in each cluster λ changes significantly across the FOV: while we get typical λ values of 1–1.3, the standard deviation across the FOV is of order $\sim$0.4—again showing that MST is not the main reason for the differences between the methods.

3. Examining the individual MST-corrected maps, compared to the original LTM maps, we see that the isodensity contours—and in that sense also the effective ellipticity, as well as the critical curves—remain identical to the original maps (as expected; see Schneider & Sluse 2013). This once more shows that the difference between the maps cannot be attributed to MST. Instead, as can be seen immediately from Figures 3–4 (see the extended, online version showing all clusters), the main difference arises from a different ellipticity of the mass distributions.

4. In addition, the MST-corrected maps often exhibit unrealistic properties, such as $\kappa < 0$ at as near as a few θ_e from the center, where this cannot be reasonable (e.g., we know from independent, larger-scale lensing analyses that this

is definitely not the case). These unrealistic values indeed (mathematically) help reduce the systematic differences between the integrated mass *profiles* (to $\lesssim$10%) and average magnifications (can improve the differences by a factor of $\sim$2), but these are physically unreasonable corrections and, as was shown above, meaningless here.

We therefore conclude that MST cannot account for the differences between the mass models from the two methods employed here. We remain with the conclusion that the differences between the models apparently arise mainly from the different ellipticity of the mass maps. This could have been expected, as the MST correction does not change the shape (i.e., ellipticity) or isodensity contours of the input map (Schneider & Sluse 2013). In that sense it is worth noting also that the inclusion of an external shear—or the ellipticity degeneracy—is a different degeneracy than the MST. If the ellipticity degeneracy were a particular case of the MST, we should have found that the external shear should be equal to a constant times the intrinsic shear, across the FOV, i.e., it could be described as $\gamma_{\mathrm{ext.}} = k\gamma$, where k is a constant. This is clearly not the case here: γ has a typical standard deviation of $\gtrsim$0.1 from several maps we checked by eye. We conclude that the ellipticity degeneracy therefore controls the systematic differences here and seems to be a prominent systematic uncertainty in SL+WL analyses of galaxy clusters more generally, as shown in this work.

5.4. A Note on Online Availability and Future Work

As we specified, both a comparison of our lensing 2D-integrated mass profiles (Figure 9) and the Einstein radius distributions, respectively, will be used in two upcoming works to examine their consistency with wide-field WL analyses (K. Umetsu et al., in preparation) and with numerical simulations (M. Meneghetti et al., in preparation). The comparison to independent mass profiles from wide-field WL data will both help test which of the two models agrees better with the larger-field WL data and will include also an overall fit to the lens models to establish, e.g., the concentration–mass relation. The comparison with numerical simulations will both examine the sample lensing and mass properties in comparison to ΛCDM to check for consistency and can help shed light on the underlying ellipticities of the matter distributions of CLASH-like clusters. Such comparisons will also be interesting to test for agreement with halo virilization times from simulations or baryonic versus DM content and shape.

In that sense, it is important to mention that ellipticity could also, in principle, be added in the LTM parameterization directly into the mass distribution, rather than as an external shear. For example, in Zitrin et al. (2013b) we analyzed the CLASH cluster M0416 with the LTM parameterization, but with no external shear. Instead, ellipticity was embedded directly into the DM distribution by smoothing the galaxy component with an elliptical Gaussian kernel (instead of a circular one; see Section 3.1). If the underlying ellipticities of CLASH-like cluster, for example, are found eventually to be more elongated than can be described by our present LTM analysis, then it would be worth exploring further such alternative prescriptions.

It is worthwhile to mention that any lensing analysis generally calls for a possible future improvement. With time, clusters are likely to gain more exposures with *HST*, more multiple images can be uncovered, and spectroscopy may be obtained for multiple images that lack accurate redshifts. All these new data will of course help to refine the lens models even

further. However, even prior to that, any lens model is also user-dependent and can be practically always (even slightly) improved when probing a larger and more refined parameter space. Given the volume of this work, i.e., analyzing 25 clusters with two different techniques, while finding in many of them new multiple images, it is reasonable to assume that—in contrast maybe to a work devoted to one single cluster—there is room for future refinements of the models. Also, because we compare two methods, we tried as much as possible to minimize the user intervention (e.g., a few refinement iterations of the models are generally needed, following our past experience), so that models are, roughly, a direct and "nearly blind" result of the two analysis pipelines for a similar set of input constraints. Recently, we have uploaded to the MAST archive lens models for all CLASH clusters. These have been later revised, and the newer versions are those included in this work. The models being included here are being uploaded online to the MAST archive as our V2 (*HST*, SL+WL), CLASH lens models for the community. It is possible that newer versions will be supplied in the future in the same format presented here, and potential users will be thus referred to this work for details.

Last, we would like to emphasize again (see Section 5.1.4) that the *statistical* errors here were optimized to account simultaneously for the SL and WL signals. They therefore do not contain an account for other realistic sources of error, such as contribution from foreground and background LSS, etc. We advise for those directly using our models available online to adopt as nominal errors the *systematic* errors we found in this work for a more responsible error budget.

On the same matter, it would be very useful to check in a future study how much the WL data actually add to (or affect) the overall fit, which is particularly interesting to examine in the *HST* WL regime (i.e., beyond the SL regime, well outside the Einstein radius) to see if the WL constraints refine the outer mass profile, for example. Due to the extent of this work we do not attempt to thoroughly pursue that study here, which would require remodeling the full sample with only SL data for comparison, but as a preliminary, general test we adopted one cluster from our list (MS2137) and remodeled it using both parametrizations, now without the WL input. The resulting mass profiles are seen in Figure 8. We find that the PIEMDeNFW model is not significantly altered by omitting the WL data, but the (more free-form profile shape) LTM mass profile did significantly change beyond the SL regime. The LTM model that did include the WL measurements is much closer to the PIEMDeNFW profiles than the LTM model that did not include the WL data. The mass–density profile of the LTM model with no WL data differs on average by 22% from the PIEMDeNFW mass–density profile and by 12% from the LTM model that also included the WL data, in the radial range $35''-120''$ ($35''$ corresponds to twice the Einstein radius), whereas the LTM model that also included the WL data only differs by 13% from the PIEMDeNFW kappa profile in the same radial range. This shows that at least for the LTM model, whose profile is more free than that of the PIEMDeNFW model since it is not coupled to a certain analytical form, the WL data do help refine the fit and pin down the mass profile, as could be expected. The improvement on the outer mass profile, compared to the PIEMDeNFW model (if referring to the latter as a reference), is nearly a factor of two. As a second, rapid test, we also constructed one model for this cluster using only the WL data, with the PIEMDeNFW parametrization. Although we do not show it explicitly here, we note that the resulting model has a similar mass profile throughout, where only the normalization
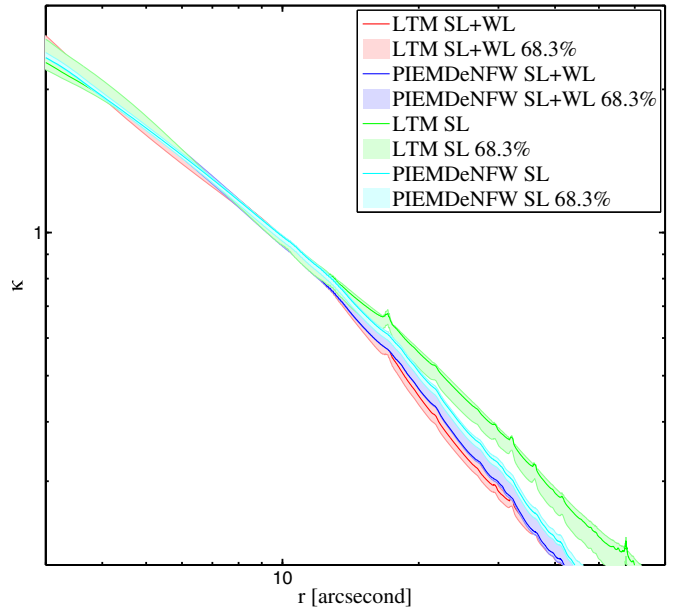

Figure 8. Effect of including the WL data, in addition to the SL data, on the resulting mass–density profile of one example cluster (MS2137), in both parameterizations. While the inclusion of *HST* WL here only mildly affects the PIEMDeNFW profile compared to its SL-only profile, it significantly affects the more free-form, LTM profile, improving it by about a factor of two in the outer radii (see Section 5.4).

is missing (as expected from the mass sheet degeneracy, broken when, e.g., adding SL constraints). Last, we used the two models for MS2137 constructed using SL constraints only, without WL information, and tested the agreement with the WL data for these. The PIEMDeNFW model agrees slightly better with the WL data than the LTM model: the WL χ^2 for the PIEMDeNFW SL-only model is $\simeq 1545$, whereas the WL χ^2 of the LTM SL-only model is only $\sim 2\%$ higher, $\simeq 1580$. For comparison, the WL χ^2 for the SL+WL models is $\simeq 1540$ for both parameterizations[23]. Assessing the effect of *HST* WL data on the overall fit for the statistical sample will also be very important for the ongoing HFF campaign, for which future versions of refined lens models will be constructed, possibly using both *HST* SL+WL deep data, in order to secure the magnification predictions beyond the SL regime. We hope to examine this more thoroughly using the full sample in a future related study.

6. SUMMARY

One of the main goals of the CLASH multicycle treasury program, set a few years ago to observe 25 mainly X-ray selected clusters, has been to study their mass distributions and related properties and confront these results with expectations for mass assembly or structure formation from ΛCDM. The CLASH program has contributed significantly to the cluster, lensing, and supernova fields (e.g., Graur et al. 2014; Patel et al. 2014; Coe et al. 2012; Monna et al. 2014; Medezinski et al. 2013; Umetsu et al. 2012; Zitrin et al. 2011b, 2012b, 2012c, 2013b), and has uncovered, through lensing, hundreds of high-redshift galaxies (e.g., Bradley et al. 2014), including some of the highest-redshift galaxies known to date (Bouwens et al. 2014; Zheng et al. 2012; Coe et al. 2013). Most recently, Merten et al. (2014) have produced the most up-to-date c-M relation derived from the CLASH

---

[23] The value differs than that in Table 1 because the test here was performed with a different, lower resolution.
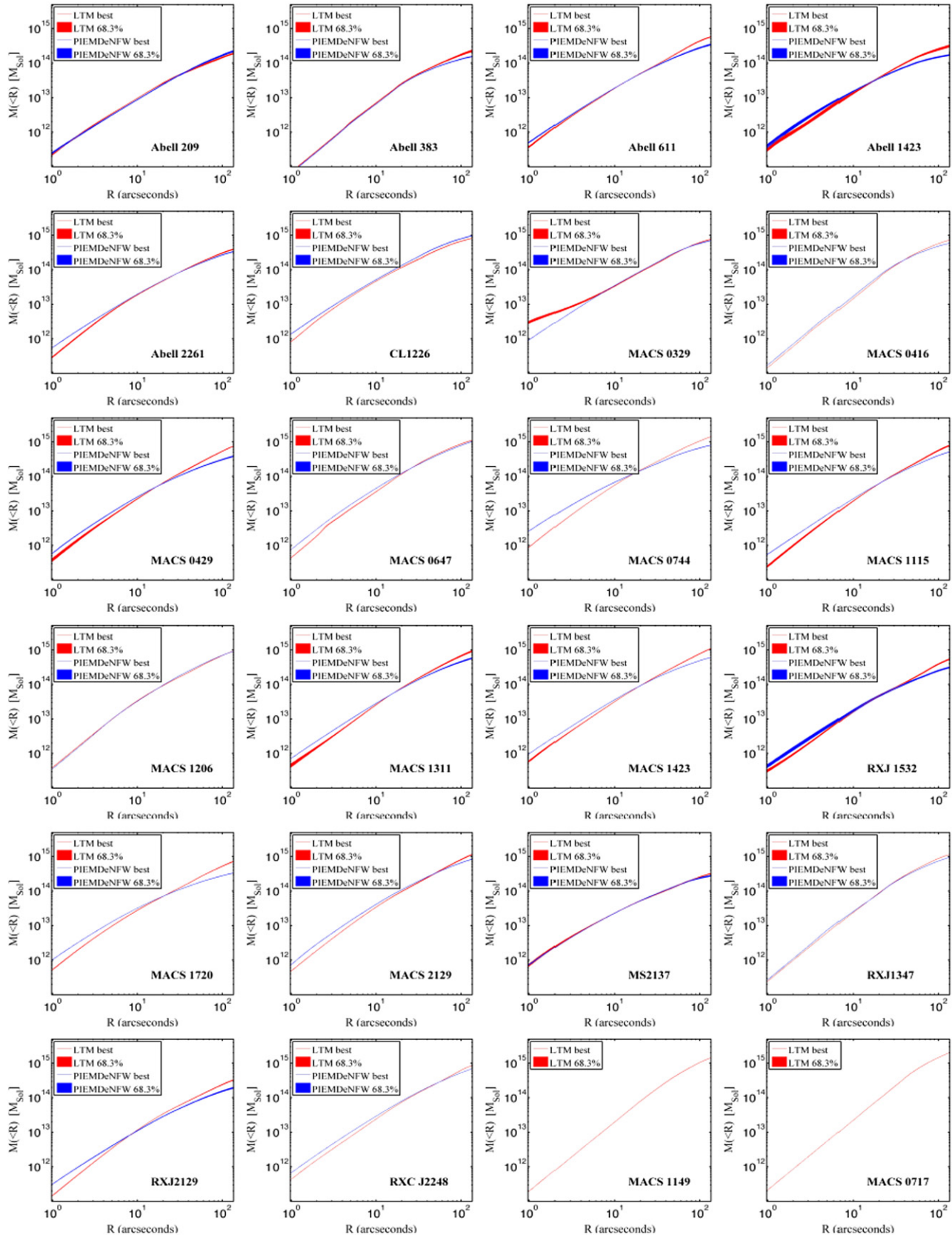
Figure 9. Integrated, 2D mass profiles for the full CLASH sample, from our *HST* SL+WL analysis described in this work. The *red* plot shows the LTM profile and errors for each cluster, and the *blue* plot shows the profile and errors of the PIEMDeNFW model. For more details, see Section 5.1.3.

sample, using nonparametric SL+WL analysis, then compared to ΛCDM simulations (Meneghetti et al. 2014), and Umetsu et al. (2014) and Donahue et al. (2014) have studied the WL and X-ray mass proxies and properties of the CLASH sample.

Aside from the treasury *HST* observations, CLASH has also been graciously granted with, or used existing, other space observations from *XMM-Newton*, *Chandra*, and *Spitzer* for X-ray and IR studies; ground-based wide-field imaging from Subaru used for wide-field WL analyses; and a dedicated VLT campaign to obtain spectroscopic redshifts for the multiple images, some of which we have presented and used in this work. Additional LBT and Keck observing times kindly granted to us in various frameworks have also enabled arc redshifts, which will be used for future refinements of the mass models.

Here we completed the high-resolution lensing analysis of the 25 CLASH clusters in the *HST* data. We incorporated both the SL features and *HST* WL shape measurements for the full sample. We make available the mass and magnification maps to the community and have characterized them in this work, with an emphasis on quantifying, in addition to the output statistical uncertainties, also the underlying systematics. To do so, we analyzed nearly all clusters with two distinct parameterizations—one adopts LTM for both galaxies and DM, while the other adopts an analytical, elliptical NFW form for the DM.

We have found that the current SL+WL data alone cannot unambiguously distinguish between an intrinsically elliptical mass distribution, or a light-tracing-mass distribution for which the overall ellipticity is introduced only in the form of an external shear not contributing to the mass distribution. These two distinct parameterizations introduce some notable discrepancies. We found that the typical (median), relative systematic differences throughout the central $[4\rlap{.}'6 \times 4\rlap{.}'6]$ analysis FOV are ∼40% in the (dimensionless) mass density, κ, and ∼20% in the magnification, μ. We showed maps of these differences for each cluster, as well as the mass distributions, critical curves, and 2D-integrated mass profiles. The Einstein radii ($z_s = 2$) typically agree within 10% between the two models, and Einstein masses agree, typically, within ∼15%. At larger radii, the total projected, 2D-integrated mass profiles of the two models, within $r \sim 2'$, differ by ∼30%. Stacking the surface-density profiles of the sample from the two methods together, we obtain an average slope of $d \log(\Sigma)/d \log(r) \sim -0.64 \pm 0.1$, in the radial range [5, 350] kpc.

Our publicly available models and the errors we find here, we hope should be most useful for future high-impact studies of lensing clusters and the objects behind them. A comparison of the sample's statistical properties, for example, of the Einstein radius distribution with ΛCDM, or the agreement of our mass profile with wider-field independent WL analyses, remains for future work.

REFERENCES

Abdelsalam, H. M., Saha, P., & Williams, L. L. R. 1998, MNRAS, 294, 734
Abell, G. O., Corwin, H. G., Jr., & Olowin, R. P. 1989, ApJS, 70, 1
Allen, S. W., Rapetti, D. A., Schmidt, R. W., et al. 2008, MNRAS, 383, 879
Ammons, S. M., Wong, K. C., Zabludoff, A. I., & Keeton, C. R. 2014, ApJ, 781, 2
Atek, H., Richard, J., Kneib, J.-P., et al. 2014a, arXiv:1409.0512
Atek, H., Richard, J., Kneib, J.-P., et al. 2014b, ApJ, 786, 60
Balestra, I., Vanzella, E., Rosati, P., et al. 2013, A&A, 559, L9
Bartelmann, M. 1995, A&A, 303, 643
Bartelmann, M. 2010, CQGra, 27, 233001
Bartelmann, M., & Schneider, P. 2001, PhR, 340, 291
Belli, S., Jones, T., Ellis, R. S., & Richard, J. 2013, ApJ, 772, 141
Benítez, N. 2000, ApJ, 536, 571
Biviano, A., Rosati, P., Balestra, I., et al. 2013, A&A, 558, A1
Bouwens, R., Bradley, L., Zitrin, A., et al. 2014, ApJ, 795, 126
Bradač, M., Clowe, D., Gonzalez, A. H., et al. 2006, ApJ, 652, 937
Bradač, M., Schrabback, T., Erben, T., et al. 2008, ApJ, 681, 187
Bradley, L. D., Zitrin, A., Coe, D., et al. 2014, ApJ, 792, 76
Broadhurst, T., Benítez, N., Coe, D., et al. 2005, ApJ, 621, 53
Broadhurst, T., Umetsu, K., Medezinski, E., Oguri, M., & Rephaeli, Y. 2008, ApJL, 685, L9
Broadhurst, T. J., & Barkana, R. 2008, MNRAS, 390, 1647
Chang, C., Jarvis, M., Jain, B., et al. 2013, MNRAS, 434, 2121
Christensen, L., Richard, J., Hjorth, J., et al. 2012, MNRAS, 427, 1953
Coe, D., Benítez, N., Broadhurst, T., & Moustakas, L. A. 2010, ApJ, 723, 1678
Coe, D., Benítez, N., Sánchez, S. F., et al. 2006, AJ, 132, 926
Coe, D., Bradley, L., & Zitrin, A. 2014, ApJ, in press (arXiv:1405.0011)
Coe, D., Fuselier, E., Benítez, N., et al. 2008, ApJ, 681, 814
Coe, D., Umetsu, K., Zitrin, A., et al. 2012, ApJ, 757, 22
Coe, D., Zitrin, A., Carrasco, M., et al. 2013, ApJ, 762, 32
Comerford, J. M., & Natarajan, P. 2007, MNRAS, 379, 190
Dahle, H., Kaiser, N., Irgens, R. J., Lilje, P. B., & Maddox, S. J. 2002, ApJS, 139, 313
D'Aloisio, A., & Natarajan, P. 2011, MNRAS, 411, 1628
Diego, J. M., Broadhurst, T., Benitez, N., et al. 2015a, MNRAS, 446, 683
Diego, J. M., Broadhurst, T., Molnar, S. M., Lam, D., & Lim, J. 2015b, MNRAS, 447, 3130
Diego, J. M., Broadhurst, T., Zitrin, A., et al. 2014, arXiv:1410.7019
Diego, J. M., Protopapas, P., Sandvik, H. B., & Tegmark, M. 2005, MNRAS, 360, 477
Donahue, M., Voit, G. M., Mahdavi, A., et al. 2014, ApJ, 794, 136
Donnarumma, A., Ettori, S., Meneghetti, M., & Moscardini, L. 2009, MNRAS, 398, 438
Donnarumma, A., Ettori, S., Meneghetti, M., et al. 2011, A&A, 528, A73
Ebeling, H., Barrett, E., & Donovan, D. 2004, ApJL, 609, L49
Ebeling, H., Barrett, E., Donovan, D., et al. 2007, ApJL, 661, L33
Ebeling, H., Edge, A. C., & Henry, J. P. 2001, ApJ, 553, 668
Ebeling, H., Edge, A. C., Mantz, A., et al. 2010, MNRAS, 407, 83
Ebeling, H., Ma, C. J., Kneib, J., et al. 2009, MNRAS, 395, 1213
Falco, E. E., Gorenstein, M. V., & Shapiro, I. I. 1985, ApJL, 289, L1
Gavazzi, R., Fort, B., Mellier, Y., Pelló, R., & Dantel-Fort, M. 2003, A&A, 403, 11
Graur, O., Rodney, S. A., Maoz, D., et al. 2014, ApJ, 783, 28
Grillo, C., Suyu, S. H., Rosati, P., et al. 2014, arXiv:1407.7866
Gruen, D., Brimioulle, F., Seitz, S., et al. 2013, MNRAS, 432, 1455
Gruen, D., Seitz, S., Brimioulle, F., et al. 2014, MNRAS, 442, 1507
Halkola, A., Hildebrandt, H., Schrabback, T., et al. 2008, A&A, 481, 65
Hoekstra, H., & Jain, B. 2008, ARNPS, 58, 99
Host, O. 2012, MNRAS, 420, L18
Ishigaki, M., Kawamata, R., Ouchi, M., et al. 2015, ApJ, 799, 12
Jauzac, M., Clément, B., Limousin, M., et al. 2014, MNRAS, 443, 1549
Jauzac, M., Jullo, E., Kneib, J.-P., et al. 2012, MNRAS, 426, 3369
Jee, M. J., & Tyson, J. A. 2009, ApJ, 691, 1337
Johnson, T. L., Sharon, K., Bayliss, M. B., et al. 2014, ApJ, 797, 48
Jouvel, S., Host, O., Lahav, O., et al. 2014, A&A, 562, A86
Jullo, E., Kneib, J.-P., Limousin, M., et al. 2007, NJPh, 9, 447
Jullo, E., Natarajan, P., Kneib, J., et al. 2010, Sci, 329, 924
Kaiser, N., Squires, G., & Broadhurst, T. 1995, ApJ, 449, 460
Kelly, P., Rodney, S., Treu, T., et al. 2014, arXiv:1405.6099

Kneib, J.-P., Ellis, R. S., Santos, M. R., & Richard, J. 2004, ApJ, 607, 697
Kneib, J.-P., Ellis, R. S., Smail, I., Couch, W. J., & Sharples, R. M. 1996, ApJ, 471, 643
Kneib, J. P., Mellier, Y., Fort, B., & Mathez, G. 1993, A&A, 273, 367
Kneib, J.-P., & Natarajan, P. 2011, A&ARv, 19, 47
Koekemoer, A. M., Faber, S. M., Ferguson, H. C., et al. 2011, ApJS, 197, 36
Köhlinger, F., & Schmidt, R. W. 2014, MNRAS, 437, 1858
Laporte, N., Streblyanska, A., Clement, B., et al. 2014, A&A, 562, L8
Liesenborgs, J., & De Rijcke, S. 2012, MNRAS, 425, 1772
Liesenborgs, J., De Rijcke, S., & Dejonghe, H. 2006, MNRAS, 367, 1209
Liesenborgs, J., de Rijcke, S., Dejonghe, H., & Bekaert, P. 2008, MNRAS, 389, 415
Limousin, M., Ebeling, H., Ma, C.-J., et al. 2010, MNRAS, 405, 777
Limousin, M., Ebeling, H., Richard, J., et al. 2012, A&A, 544, A71
Limousin, M., Richard, J., Jullo, E., et al. 2007, ApJ, 668, 643
Limousin, M., Richard, J., Kneib, J., et al. 2008, A&A, 489, 23
Lotz, J., Mountain, M., Grogin, N. A., et al. 2014, in American Astronomical Society Meeting Abstracts, 223, 254.01
Mann, A. W., & Ebeling, H. 2012, MNRAS, 420, 2120
Marshall, P., Rajguru, N., & Slosar, A. 2006, PhRvD, 73, 067302
Massey, R., & Goldberg, D. M. 2008, ApJL, 673, L111
Maughan, B. J., Jones, C., Forman, W., & Van Speybroeck, L. 2008, ApJS, 174, 117
Maughan, B. J., Jones, C., Jones, L. R., & Van Speybroeck, L. 2007, ApJ, 659, 1125
Medezinski, E., Umetsu, K., Nonino, M., et al. 2013, ApJ, 777, 43
Meneghetti, M., Fedeli, C., Zitrin, A., et al. 2011, A&A, 530, A17
Meneghetti, M., Rasia, E., Vega, J., et al. 2014, ApJ, 797, 34
Merten, J., Cacciato, M., Meneghetti, M., Mignone, C., & Bartelmann, M. 2009, A&A, 500, 681
Merten, J., Coe, D., Dupke, R., et al. 2011, MNRAS, 417, 333
Merten, J., Meneghetti, M., Postman, M., et al. 2014, arXiv:1404.1376
Monna, A., Seitz, S., Greisel, N., et al. 2014, MNRAS, 438, 1417
Narayan, R., & Bartelmann, M. 1996, arXiv:astro-ph/9606001
Navarro, J. F., Frenk, C. S., & White, S. D. M. 1996, ApJ, 462, 563
Newman, A. B., Treu, T., Ellis, R. S., & Sand, D. J. 2011, ApJL, 728, L39
Newman, A. B., Treu, T., Ellis, R. S., & Sand, D. J. 2013a, ApJ, 765, 25
Newman, A. B., Treu, T., Ellis, R. S., et al. 2009, ApJ, 706, 1078
Newman, A. B., Treu, T., Ellis, R. S., et al. 2013b, ApJ, 765, 24
Nordin, J., Rubin, D., Richard, J., et al. 2014, MNRAS, 440, 2742
Oguri, M., Bayliss, M. B., Dahle, H., et al. 2012, MNRAS, 420, 3213
Oguri, M., Schrabback, T., Jullo, E., et al. 2013, MNRAS, 429, 482
Okabe, N., Takada, M., Umetsu, K., Futamase, T., & Smith, G. P. 2010, PASJ, 62, 811

Patel, B., McCully, C., Jha, S. W., et al. 2014, ApJ, 786, 9
Paulin-Henriksson, S., Antonuccio-Delogu, V., Haines, C. P., et al. 2007, A&A, 467, 427
Postman, M., Coe, D., Benítez, N., et al. 2012, ApJS, 199, 25
Rau, S., Vegetti, S., & White, S. D. M. 2014, MNRAS, 443, 957
Rhodes, J., Refregier, A., & Groth, E. J. 2000, ApJ, 536, 79
Rhodes, J. D., Massey, R. J., Albert, J., et al. 2007, ApJS, 172, 203
Richard, J., Jauzac, M., Limousin, M., et al. 2014, MNRAS, 444, 268
Richard, J., Kneib, J.-P., Ebeling, H., et al. 2011, MNRAS, 414, L31
Richard, J., Smith, G. P., Kneib, J.-P., et al. 2010, MNRAS, 404, 325
Sand, D. J., Treu, T., Ellis, R. S., Smith, G. P., & Kneib, J. 2008, ApJ, 674, 711
Sand, D. J., Treu, T., Smith, G. P., & Ellis, R. S. 2004, ApJ, 604, 88
Schindler, S., Guzzo, L., Ebeling, H., et al. 1995, A&A, 299, L9
Schmidt, R. W., & Allen, S. W. 2007, MNRAS, 379, 209
Schneider, P., & Sluse, D. 2013, A&A, 559, A37
Sereno, M., Ettori, S., Umetsu, K., & Baldi, A. 2013, MNRAS, 428, 2241
Smith, G. P., Ebeling, H., Limousin, M., et al. 2009, ApJL, 707, L163
Smith, G. P., Kneib, J., Ebeling, H., Czoske, O., & Smail, I. 2001, ApJ, 552, 493
Smith, G. P., Kneib, J., Smail, I., et al. 2005, MNRAS, 359, 417
Umetsu, K., Birkinshaw, M., Liu, G.-C., et al. 2009, ApJ, 694, 1643
Umetsu, K., Broadhurst, T., Zitrin, A., Medezinski, E., & Hsu, L. 2011a, ApJ, 729, 127
Umetsu, K., Broadhurst, T., Zitrin, A., et al. 2011b, ApJ, 738, 41
Umetsu, K., Medezinski, E., Broadhurst, T., et al. 2010, ApJ, 714, 1470
Umetsu, K., Medezinski, E., Nonino, M., et al. 2012, ApJ, 755, 56
Umetsu, K., Medezinski, E., Nonino, M., et al. 2014, ApJ, 795, 163
Vanzella, E., Fontana, A., Zitrin, A., et al. 2014, ApJL, 783, L12
Zheng, W., Postman, M., Zitrin, A., et al. 2012, Natur, 489, 406
Zheng, W., Shu, X., Moustakas, J., et al. 2014, ApJ, 795, 93
Zitrin, A., & Broadhurst, T. 2009, ApJL, 703, L132
Zitrin, A., Broadhurst, T., Barkana, R., Rephaeli, Y., & Benítez, N. 2011a, MNRAS, 410, 1939
Zitrin, A., Broadhurst, T., Bartelmann, M., et al. 2012a, MNRAS, 423, 2308
Zitrin, A., Broadhurst, T., Coe, D., et al. 2011b, ApJ, 742, 117
Zitrin, A., Broadhurst, T., Rephaeli, Y., & Sadeh, S. 2009a, ApJL, 707, L102
Zitrin, A., Broadhurst, T., Umetsu, K., et al. 2009b, MNRAS, 396, 1985
Zitrin, A., Broadhurst, T., Umetsu, K., et al. 2010, MNRAS, 408, 1916
Zitrin, A., Menanteau, F., Hughes, J. P., et al. 2013a, ApJL, 770, L15
Zitrin, A., Meneghetti, M., Umetsu, K., et al. 2013b, ApJL, 762, L30
Zitrin, A., Moustakas, J., Bradley, L., et al. 2012b, ApJL, 747, L9
Zitrin, A., Rosati, P., Nonino, M., et al. 2012c, ApJ, 749, 97
Zitrin, A., Zheng, W., Broadhurst, T., et al. 2014, ApJL, 793, L12